

Award Number: W81XWH-09-1-0299

TITLE: Photoacoustic Imaging of Epilepsy

PRINCIPAL INVESTIGATOR: Huabei Jiang, PhD

CONTRACTING ORGANIZATION:

Á
University of Florida
Gainesville, FL 32611

REPORT DATE: April 2013

TYPE OF REPORT: Annual

PREPARED FOR: U.S. Army Medical Research and Materiel Command
Fort Detrick, Maryland 21702-5012

DISTRIBUTION STATEMENT: (Check one)

- Approved for public release; distribution unlimited
- Distribution limited to U.S. Government agencies only;
report contains proprietary information

The views, opinions and/or findings contained in this report are those of the author(s) and should not be construed as an official Department of the Army position, policy or decision unless so designated by other documentation.

REPORT DOCUMENTATION PAGE

Form Approved
OMB No. 0704-0188

Public reporting burden for this collection of information is estimated to average 1 hour per response, including the time for reviewing instructions, searching existing data sources, gathering and maintaining the data needed, and completing and reviewing this collection of information. Send comments regarding this burden estimate or any other aspect of this collection of information, including suggestions for reducing this burden to Department of Defense, Washington Headquarters Services, Directorate for Information Operations and Reports (0704-0188), 1215 Jefferson Davis Highway, Suite 1204, Arlington, VA 22202-4302. Respondents should be aware that notwithstanding any other provision of law, no person shall be subject to any penalty for failing to comply with a collection of information if it does not display a currently valid OMB control number. **PLEASE DO NOT RETURN YOUR FORM TO THE ABOVE ADDRESS.**

| | | | | | |
|--|-------------------------|---------------------------------|---|--|---|
| 1. REPORT DATE (DD-MM-YYYY) April 2013 | | 2. REPORT TYPE Annual | | 3. DATES COVERED (From - To) 01 April 2012-30 March 2013 | |
| 4. TITLE AND SUBTITLE Photoacoustic Imaging of Epilepsy | | | | 5a. CONTRACT NUMBER | |
| | | | | 5b. GRANT NUMBER W81XWH-09-1-0299 | |
| | | | | 5c. PROGRAM ELEMENT NUMBER | |
| 6. AUTHOR(S) Huabei Jiang, PhD | | | | 5d. PROJECT NUMBER | |
| | | | | 5e. TASK NUMBER | |
| | | | | 5f. WORK UNIT NUMBER | |
| 7. PERFORMING ORGANIZATION NAME(S) AND ADDRESS(ES) University of Florida Gainesville, FL 32611 | | | | 8. PERFORMING ORGANIZATION REPORT NUMBER | |
| 9. SPONSORING / MONITORING AGENCY NAME(S) AND ADDRESS(ES) U.S. Army Medical Research and Materiel Command Fort Detrick, Maryland | | | | 10. SPONSOR/MONITOR'S ACRONYM(S) | |
| | | | | 11. SPONSOR/MONITOR'S REPORT NUMBER(S) | |
| 12. DISTRIBUTION / AVAILABILITY STATEMENT Approved for public release; distribution unlimited | | | | | |
| 13. SUPPLEMENTARY NOTES | | | | | |
| 14. ABSTRACT This research is aimed at developing a new imaging approach, called "Photoacoustic tomography (PAT)", for non-invasively tracking dynamical changes during seizure occurrence. The project will develop imaging hardware and software, and conduct phantom/in vivo experiments to achieve the proposed goals. During the fourth year of this project, We have developed and validated a rat model of temporal lobe epilepsy. We have performed extensive <i>in vivo</i> experiments to achieve concurrent EEG and PAT recordings. Interesting results are obtained that may be significant for seizure prediction and for neurovascular coupling studies. We have designed and constructed a light-weighted animal/transducer interface that can be used for chronic monitoring of freely moving animals. | | | | | |
| 15. SUBJECT TERMS Photoacoustic imaging, photoacoustic tomography, epilepsy, seizure | | | | | |
| 16. SECURITY CLASSIFICATION OF: | | | 17. LIMITATION OF ABSTRACT UU | 18. NUMBER OF PAGES 67 | 19a. NAME OF RESPONSIBLE PERSON USAMRMC |
| a. REPORT U | b. ABSTRACT U | c. THIS PAGE U | | | 19b. TELEPHONE NUMBER (include area code) |

Table of Contents

| | <u>Page</u> |
|--|-------------|
| Introduction..... | 1 |
| Body..... | 1 |
| Key Research Accomplishments..... | 11 |
| Reportable Outcomes..... | 11 |
| Conclusion..... | 11 |
| References..... | |
| Appendices..... | 12 |

Introduction

Approximately 2.5 million Americans live with epilepsy and epilepsy-related deficits today, more than disabled by Parkinson disease or brain tumors. The impact of epilepsy in the US is significant with a total cost to the nation for seizures and epilepsy of approximately \$12.5 billion. Epilepsy consists of more than 40 clinical syndromes affecting 40 million people worldwide. Approximately 25 percent of individuals receiving antiepileptic medication have inadequate seizure control; however, 80% individuals with medication resistant epilepsy might be cured through surgery if one were able to precisely localize the seizure focus. The proposed research will significantly advance our ability to localize such foci, and thereby offer curative epilepsy surgery for this devastating disease. Photoacoustic tomography (PAT) uniquely combines the high contrast advantage of optical imaging and the high resolution advantage of ultrasound imaging in a single modality. In addition to high resolution structural information, the proposed PAT is also able to provide functional information that are strongly correlated with regional or focal seizure activity, including blood volume and blood oxygenation because of the high sensitivity of optical contrast to oxyhemoglobin and deoxyhemoglobin concentrations. The hypothesis of the proposed research is that PAT offers the possibility to non-invasively track dynamical changes during seizure occurrence. The overall goal of this research is to advance a finite element based photoacoustic tomography method for epilepsy imaging, using both laboratory and in vivo experiments. Specifically, in this project we propose: (1) To design, construct and test a transducer array system for both 2D and 3D PAT imaging; (2) To advance reconstruction algorithms and associated image enhancement schemes for quantitative PAT; (3) To evaluate and optimize the integrated functioning of the hardware and software components of the transducer array-based system, using simulation and phantom experiments; (4) To test and validate the PAT system using a well established animal model of temporal lobe epilepsy.

Body

This report describes work accomplished in Year 4 (Months 37-48) of the project. As outlined in the approved Statement of Work (SOW), the tasks during this period of time include: **Task 6.** Months 25-42: Develop a rat temporal lobe epilepsy animal model; Conduct animal experiments for evaluating the PAT imaging system/Record EEG and PAT concurrently in animal model; Preparation for chronic monitoring/imaging of animals.

The sections below consist of (1) rat model of temporal lobe epilepsy, (2) animal experiments, and (3) Preparation for chronic monitoring/imaging of animals that reflect the tasks associated with the SOW during Months 37-48.

1. Rat Model of Temporal Lobe Epilepsy

During months 37-48 of this project, we have successfully developed and validated the rat model of temporal lobe epilepsy as follows:

Animal preparation:

Experiments were performed on 2-month old male Sprague Dawley rats ($n = 4$) weighing 210–265 g using protocols and procedures approved by the University of Florida Institutional Animal Care and Use Committee. Anesthesia was initiated with xylazine (10 mg/kg, SQ) and isoflurane (1–3%) in oxygen, animals were placed in a Kopf stereotactic frame, and inhalation anesthesia was continued via a nose mask.

Electrode implantation:

The top of the animal's head was shaved and chemically sterilized with iodine. The skull was exposed by a midsagittal incision that began between the eyes and extended caudally to the level of the ears to expose the bregma and lambdoidal suture. A peroxide wash was applied to remove excess soft tissue from the skull. Four 0.8 mm stainless steel screws (Small Parts, Miami Lakes, FL) were placed in the skull to anchor the acrylic headset: 1) two screws were AP 2 mm and bilaterally 2 mm; 2) one screw was AP-3 mm and left 2 mm and served as a ground electrode; and 3) one screw was AP-2 mm to the lambdoidal suture and right 2 mm and served as a reference electrode. Holes were drilled to permit insertion of 2 stainless steel bipolar twist electrodes (1 mm tip separation) into the left and right ventral hippocampi for electrical stimulation and recording (AP-5.3 mm, bilateral 4.9 mm, vertical-5 mm below the dura) and 2 stainless steel monopolar recording electrodes in the bilateral frontal cortices (AP 3.2 mm, bilateral 1 mm, vertical-2.5 mm below the dura). Electrodes were labeled according to their relative positions on the rat's skull as LF/RF (left/right frontal) and LH/RH (left/right hippocampus). Electrode pins were positioned in a plastic strip connector and the entire headset was glued into place using cranioplast cement (Plastics One, Inc., Roanoke, VA). Following surgery, animals were allowed to recover for a week prior to additional procedures.

Induction of seizures:

Animals underwent hippocampal stimulation one week after surgery to induce status epilepticus. The left ventral hippocampus was stimulated in all animals. During electrical stimulation and iEEG acquisition, animals were housed in in-house specially-made chambers. Stimulus trains were delivered for 50-70 min with a duty cycle of 10 s on and 2 s off consisting of biphasic square wave pulses at a frequency of 50 Hz, a pulse duration of 1 ms, and intensities of 300-400 μ A. During the stimulus, a normal behavioral response was for the animal to display "wet dog shakes" and increased exploratory activity. After approximately 20-30 min of stimulation, convulsive seizures (up to 1 min in duration) were usually observed about every 10 min. At the end of the stimulus period, continuous iEEG recordings were observed for evidence of slow waves in all recorded channels. If slow waves were not demonstrated, then the stimulus was re-applied for 10-min intervals 1-3 times until continuous slow waves appeared following termination of the stimulus. According to our experience, lack of response to this stimulation protocol was infrequent (< 10% of animals) and was attributed, in part, to inaccurate placement of the stimulating electrode in the ventral hippocampus. Upon termination of continuous hippocampal stimulation, the iEEG continued to demonstrate activity below 5 Hz for 12-24 h and intermittent spontaneous 30-60 s electrographic seizures for 2-4 h. Animals were observed for seizure activity and adequate food and water intake for 12-24 h after stimulation. Following behavioral stabilization, animals were returned to the vivarium for 6 weeks during which time spontaneous seizures developed.

Data acquisition:

Each animal was connected by a 6-channel commutator and shielded cable to the recording system, which consisted of an analog amplifier (Grass Telefactor-Model 10), a 12 bit A/D converter (National Instruments, Inc.), and recording software (HARMONIE 5.2, Stellate Inc., Montreal). The system was synchronized to a video unit for time-locked monitoring of behavioral

changes. Each channel was sampled at a uniform rate of 200 Hz after the signal was filtered using analog high and low pass filters at cutoff frequencies of 0.1 Hz and 70 Hz, respectively. The recording system used a 4-channel referential montage, and the iEEG and video data were then transferred to a 1.4 TB RAID server for subsequent off-line review and analysis.

Data characteristics, seizure detection, and classification:

Video-iEEG recordings were reviewed visually for electrographic as well as behavioral seizures. A classification scheme developed by Racine (1972) for kindled seizures was used to grade seizure activity and assign the corresponding “class.” Seizure onset was defined electrographically as the first sustained change in the iEEG that was clearly different than the background activity. Seizure offset was defined as that time when generalized high frequency epileptiform activity ceased abruptly. Seizure offset was followed by a predictable sequence of brief generalized voltage suppression, the appearance of spike and wave discharges (SWDs) at 1–2 Hz, which continued for ~30 s–1 min, and a prolonged generalized voltage suppression across all channels reflective of an actual postictal state (Fig. 1). All iEEG segments included for analysis were deemed sufficiently artifact-free by review of an electroencephalographer.

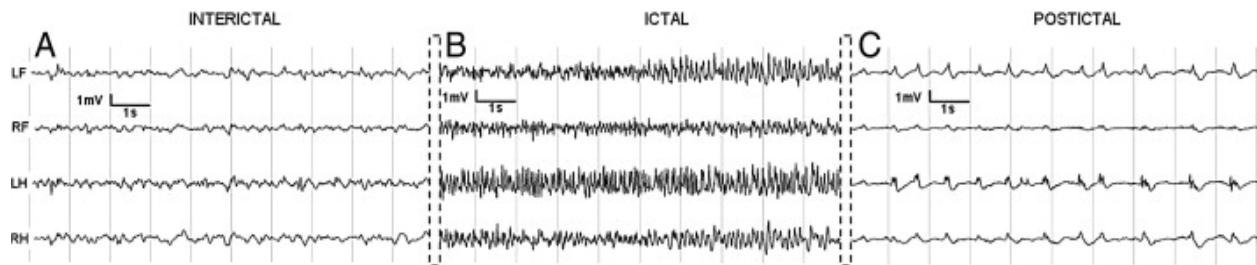


Fig. 1 Samples of 4-channel iEEG recordings of an epileptic rat during (A) interictal (B) ictal and (C) postictal periods. Interictal EEG (A) was sampled one hour before the beginning of the ictal period (B), and the postictal EEG (C) was sampled approximately 10 s after the end of the ictal EEG. LF: Left Frontal Cortex, RF: Right Frontal Cortex, LH: Left Hippocampus, RH: Right Hippocampus. Each of the displayed electrodes is connected to the skull screw reference electrode to generate the corresponding voltage trace.

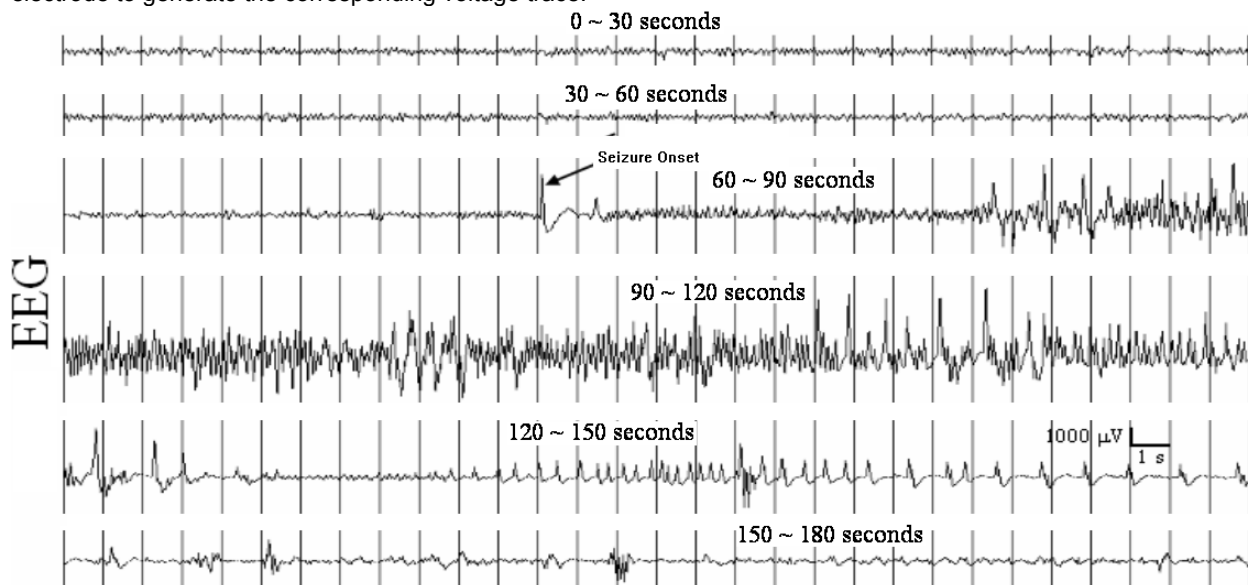


Fig. 2 Three minutes of EEG from an epileptic rat.

Three minutes of EEG (demonstrated by 6 sequential 30-second segments) data recorded from the left hippocampus, showing a sample seizure from an epileptic rat (Fig. 2).

During the course of this project, we have also developed an 'epilepsy score' classification. The rationale for developing an epilepsy grading score for each rat is that we want to use a classifier to produce an hemodynamic imaging-based classifier of seizures. The Score was developed from a dataset of 45 rats containing 8 weeks of continuous video/EEG recordings as outlined in the research protocol. The following characteristics were used to develop the Score: number of seizures,

mean seizure duration, and Racine grade (0-5). The Score was developed from a subset of 28 continuous video/EEG recordings. We obtained a distribution of Scores using the following methods: First we estimated the mean seizure rate per day NS for each rat, defined as $NS = S/D$, where S is the total number of seizures generated by the rat and D is the total duration of EEG recordings for the rat. Then we estimated the normalized Racine scale NR for the rat. Also we defined the normalized mean seizure duration $ND = T/120$, where T is the mean seizure duration measured in seconds. It has been our experience that the duration of the seizures in this rat model rarely exceeds 120 seconds. The seizure grade G for the rat is then given as: $G = (NS+NR+ND)/3$. In Fig. 3, we show the probability density $p(G)$ obtained for all the rats measured. The curve in red represents the Gaussian fit to the $p(G)$. Using this empirical estimate for $p(G)$, we define Epilepsy Scores (L: Low; M: Medium; H:High) for a given rat as L: $G < 0.5$; M: ; H:. In summary, these results indicate that the rat TLE model closely reflects human TLE in that epilepsy grades will vary amongst individuals from high to low.

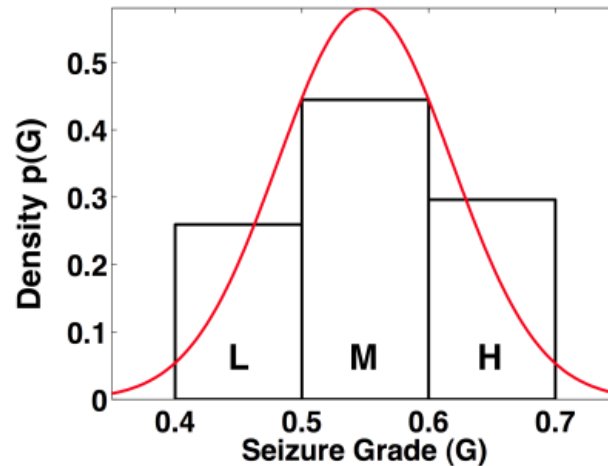


Fig. 3 Probability density.

Histological examination:

The rationale for performing histology is that we want to relate qualitatively the observed pathology to brain imaging results. After PAT imaging, the excised rat brains were cryoprotected in a 30% sucrose PBS solution for 24-48 hrs then sectioned frozen at 50 μm with a sliding microtome. Every sixth section in succession was stained with Timm's, Fluoro Jade C (FJC), Black Gold II, glial fibrillary acidic protein (GFAP), microglial (CD68 antibody), and Perl stain. All chemical reagents for histology will be purchased from Sigma Chemicals Co., (St. Louis, MO) unless otherwise noted. Timms staining was performed using the Timm sulfide silver method (58) to assess mossy fiber sprouting. In order to assess changes in myelin, the slides were stained with 0.2% Black Gold II (59). FJC staining (60) was used to visualize degenerating neurons. Some sections were stained using a modified Bielschowsky method (61) to assess degenerating neurons. Mounted sections were incubated in 20% silver nitrate solution for 15 min followed by incubation in silver nitrate/ammonium hydroxide solution in the dark for 15 min. For pathological visualization of iron, sections were incubated in Perl's solution.

Most sections were counterstained with Cresyl Violet. Sections were dehydrated and cover slipped with Eukitt (Calibrated Instruments, Ardsley, NY). The two examples below (Fig. 4) are histological examination of astrocytosis and microglial reactions, respectively, in hippocampus.

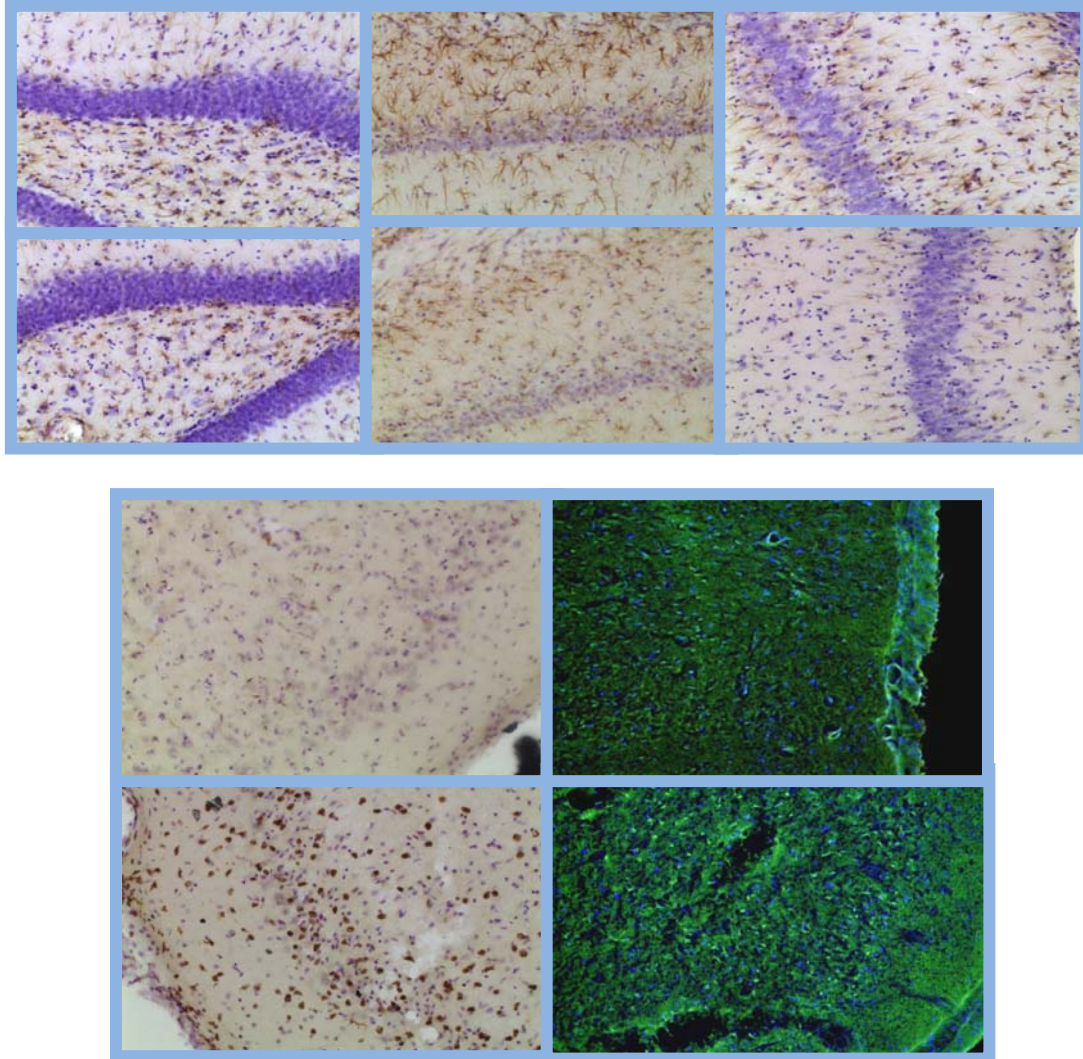


Fig. 4 Histological examination of astrocytosis and microglial reactions, respectively, in hippocampus.

Problems and limitations of procedures: One minor problem that we have encountered during long-term monitoring is the interruption or premature termination of longitudinal video-EEG data caused by the unexpected loss of an animal's electrode headset. Although headset loss has been infrequent, it has occurred secondary to scalp infection, or to mechanical dislodgement by the animal's scratching or inadvertent head impact during severe whole body myoclonic jerks, or repeated bumping of the wire-top lid of its cage. Eliminating the wire-top cage lids has solved the latter problem.

2. Animal Experiments

In Year 4 we continue to conduct extensive animal experiments to evaluate the PAT system constructed in Years 1 and 2 with an emphasis on realizing concurrent PAT and EEG recording which is critical to complete the proposed chronic monitoring of animals. The PAT system constructed has already been described in detail in previous progress reports. Briefly, the center piece of the system is a sparse spherical interface containing 192 discrete transducers, as shown in Fig. 5(a). The transducers were mounted on a custom fabricated white ABS spherical interface with a distance of 71.6mm from the center of the array, and formed into seven layers. Each transducer had a central frequency of 5MHz and a reception bandwidth of greater than 80%. The active area of the transducer was 3mm in diameter, and the angular acceptance was about 15 degree. The signal from the 192 transducers was amplified by 16 homemade preamplifier boards and coupled into a 64 channel parallel data acquisition system with 3:1 multiplexing, as indicated with three different colors in Fig. 5(a). 1064nm light from a pulsed Nd: YAG (5~20ns pulse width) was delivered through a concave lens onto the head of the rat homogenously with a light intensity about $50\text{mJ}/\text{cm}^2$, significantly below the safty standard. The laser had a repetition rate of 10Hz, allowing the system to record one complete of 3D image in 0.33s.

Two EEG electrodes were inserted into the front cortex of rat brain with about 3mm below the scalp, as shown in Fig. 5(b). One electrode served as the reference and ground, while the other electrode was used to record the EEG signal. The EEG signal was amplified (RA16PA, TDtucker-Davis Tech.) and recorded (RZ5 Bioamp Processor, TDtucker-Davis Tech.) with a sampling rate about 50kHz. Part of the laser light was sheltered to avoid direct shining on the metal electrodes, in case that the PAT signal from the electrode could strongly influence the rat brain image. Both the two electrodes were firmly glued on the rat head and the cables were tightly attached to the animal holder using glue tapes, so as to avoid noise induced by any unnecessary movement of the rat and experiment operator. The PAT system gave an output synchronization signal to the EEG system, so that the two systems were well synchronized.

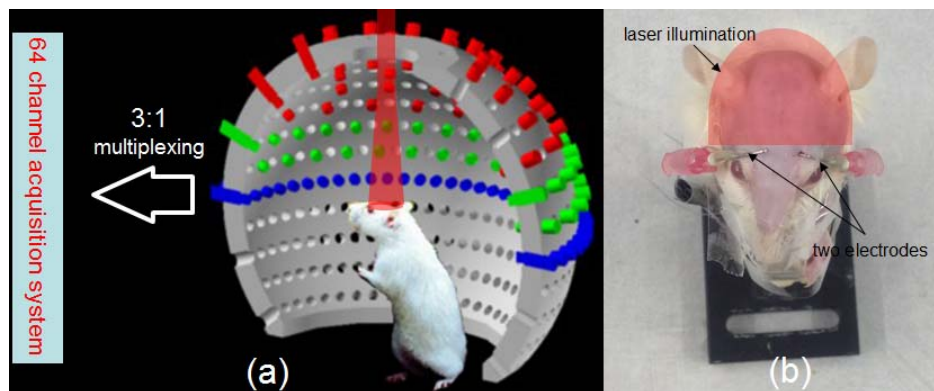


Fig. 5 (a) Schematic of the PAT system/animal interface; (b) Rat with two electrodes in the brain and laser illumination.

Both the PAT and EEG data were stored on hard disk before further data processing. With a frame rate of 3.3f/s, there were 6000 complete sets of PAT data for a 30min experimental time.

Before doing 3D image reconstruction and processing, 2D PAT images were reconstructed and checked using data collected by the 64 transducers in the lowest layer of the array, which were indicated with blue in Fig. 5(a). This was to make sure that there was not any intensive movement of the rat during the experiment. Then 3D images were calculated, and the negative values were set to zero. All PAT images were reconstructed a GPU based parallel reconstruction code.

We found that there was a strong 10Hz noise in the acquired EEG data induced by the laser and DAQ system of the PAT system. Thus for EEG data processing, we first de-noised the EEG data minute by minute by replacing the short period of noisy data with adjacent data. Then the EEG data was transformed into 30000 point data over the 30min recording period, which was then compared with the hemodynamic response computed with the PAT data.

The 2D images for a selected rat over 30min window are displayed in Fig. 6. We see that the main vein and its two branch vessels at the posterior area are clearly imaged. Some other small blood vessel structures are also revealed. We can see that there was no noticeable movement of the rat brain. Since it's hard to tell when the seizure began just by eyes, further analyze is needed.

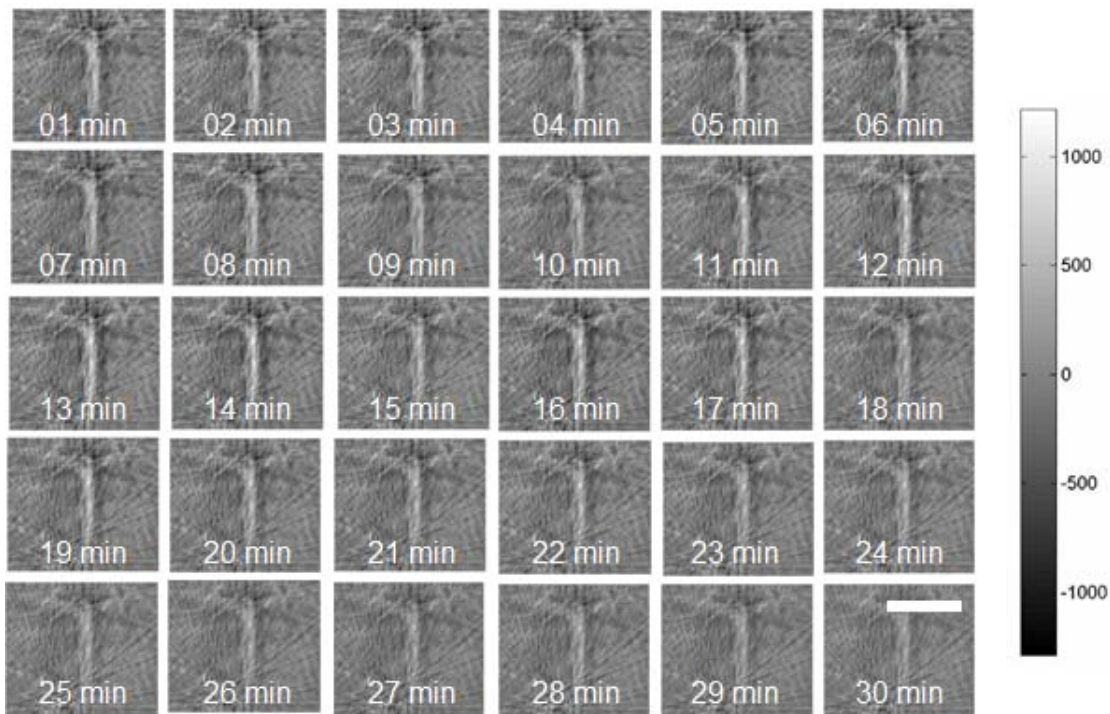


Fig. 6 2D PAT image for a selected rat over a 30min window. Each image covers 10×10 mm with 201×201 pixels. Scale bar represents 5mm.

One 3D image for the same rat is shown in Fig. 7(a). To average PAT signal of the main vein, a cubic volume that could enclose the main vein all through the experiment was chosen. Then the averaged voxel value of this cubic volume was calculated as the average PAT signal of the main vein. Then its change was calculated. It is noted that although the cubic volume is a little

bigger than the main vein, because most other voxels around the main vein have a value of zero, the averaged value of the cube is proportional to the averaged value of the main vein.

Fig. 7(b) shows a period of 2 seconds of the EEG signal for the same rat. The blue curve is the raw data, and strong 10Hz noise from the laser and DAQ system can be seen. The red curve is the EEG data after removing the noise, which attains all the features from the original data.

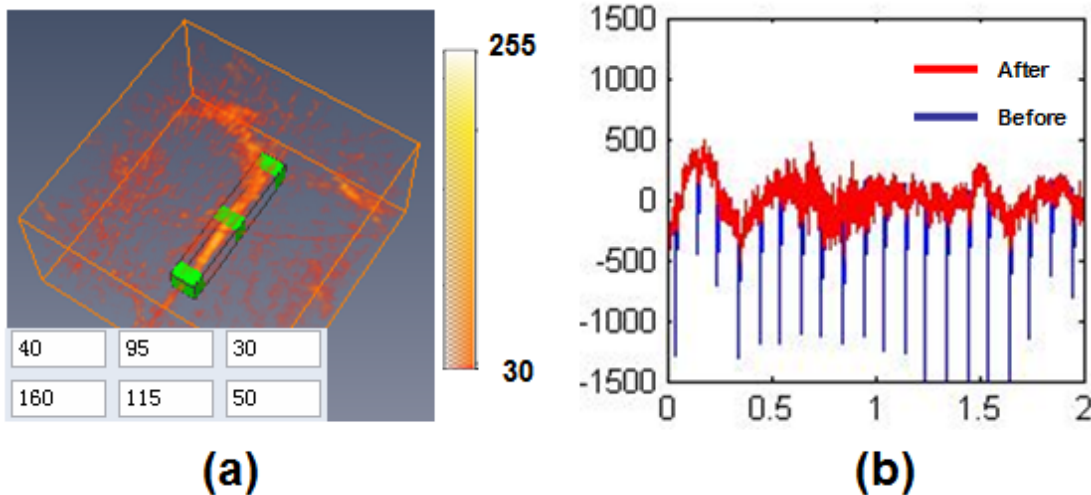


Fig. 7 Processing of the PAT and EEG data. (a) Averaged main vein signal is extracted; (b) 10Hz noise in the raw EEG data is removed.

The change of the extracted main vein PAT signal is compared with the EEG signal over the 30min window. Fig. 8 shows the two typical sets of results from two selected rats. From the EEG signal (blue curve) in Fig. 8(b), which represents the 2nd rat, we can see that intensive EEG spikes arise at 10min 5s, which is about 2min 5s after the seizure onset. Shortly before that time, dramatic change of PAT signal of the main vein has already occurred - first with a drop, then followed by increase, finally achieved its peak at about 13min. The PAT curve of the 1st rat was similar to the 2nd, only with the difference that the time gap between the first EEG spike and the beginning of PAT change is much longer (~5min).

Of the four rats studied, we notice a distinguishable change of the PAT signal consisting of a decrease followed by an increase, which takes place before the first EEG spike. This may imply that there is some hemodynamic change occurring before the first ictal event during seizure, indicating the possibility of using PAT imaging for seizure prediction. The amplitudes of the drop and increase in PAT signal were all recorded, as shown in Table. 1. We also recorded the beginning time of the PAT signal change and the time of first EEG spike, and calculated their time difference. It is noted that before the change, the PAT signals kept quite stable, only with random high frequency fluctuations. This not only means that the rat vital signs kept stable, but also means our PAT system was reliable. Thus, we could use the standard deviation of this period of PAT signal as the noise level of each experiment, which was also shown in Table. 1.

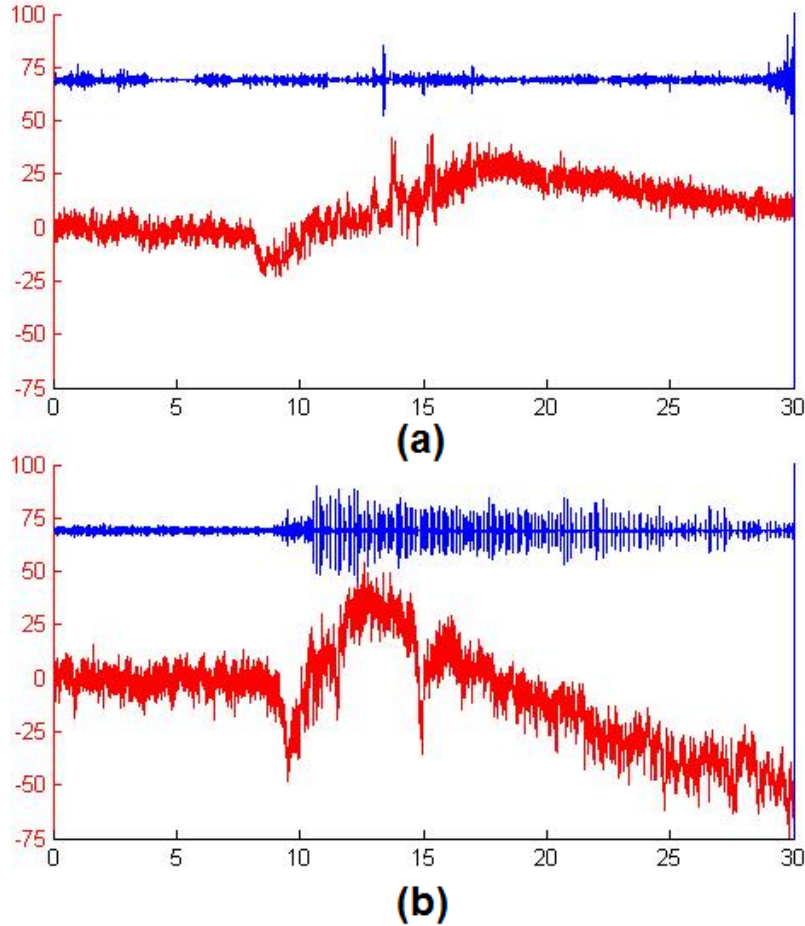


Fig. 8 PAT and EEG signal analysis for two rats. (a) & (b): PAT signal change (red) of main vein for the 1st rat (a) and 2nd rat (b) over 30min, and the corresponding EEG curves (blue). PAT curve is presented in percent, and the EEG curve is presented in arbitrary units.

Table 1 PAT and EEG data analysis for four rats

| rat | noise level(%) | first EEG spike | first PAT change | time difference | PAT decrease (%) | PAT increase (%) |
|-----|----------------|-----------------|------------------|-----------------|------------------|------------------|
| 1 | 3.5 | 13min 21s | 8min 0s | 5min 21s | 20.7 | 44.1 |
| 2 | 4.8 | 10min 5s | 7min 45s | 2min 20s | 35.0 | 47.5 |
| 3 | 2.8 | 10min 4s | 8min 24s | 1min 20s | 21.4 | 54.8 |
| 4 | 4.4 | 9min 46s | 7min 58s | 1min 47s | 20.0 | 53.3 |

We also attempted to construct a 3D correlation map for the animal data obtained. Most voxels in the correlation map were positive, implying that with the increase of blood supply after seizure onset in these areas. There were also some negative correlated areas, which are plotted by overlapping them with the 3D PAT images (Fig. 9) with colorbar indicating the thresholds. These areas might have experienced a strong decrease in oxygenation, again indicating that seizure was happening here.

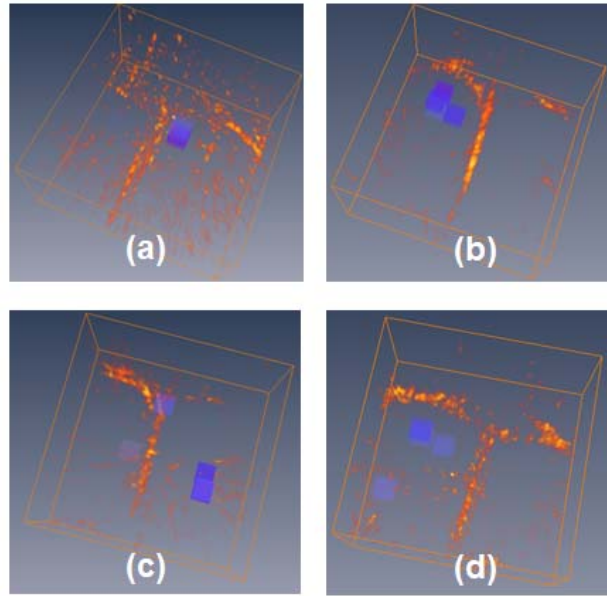


Fig. 9 Negative correlation map of the averaged voxel value with the main vein PAT signal. (a)-(d) represent the results from the 1st rat to the 4th rat, respectively.

3. Preparation for Chronic Monitoring/Imaging of Animals

In order to fulfill the proposed task of chronic monitoring epileptic rat for up to 2 months, an animal/transducer interface that can be used for freely moving animals must be constructed (the animal/transducer interface we have made and been using so far is too heavy to be used for such a purpose). A key to achieve such a cap interface is to find transducers and the associated light delivery subsystem that have light weight. After many trials and errors in Year 4, we are pleased to report that we have successfully fabricated such light-weighted transducer array (PVDF film transducers) and light delivery subsystem (plastic based light delivery). As shown in Fig. 10, a cap interface firmly attached to the rat head will allow us to chronically monitor seizure activity in freely moving rat. The cap interface weights only ~7g in total (see Fig. 10b). In Year 5 of the project (i.e., 12-month no-cost-extension), this light-weighted cap interface coupled with all other preparations described in this report will allow us to complete the proposed Tasks 6 and 7.

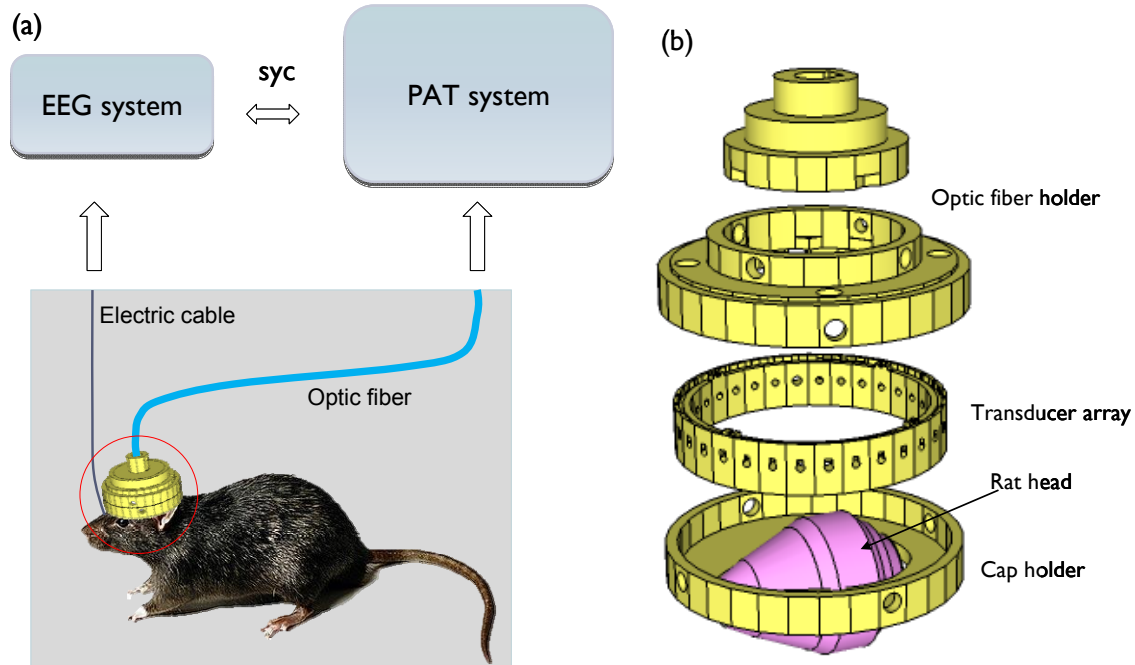


Fig. 10 (a) PAT/EEG system/cap interface for chronic monitoring/imaging of freely moving rats. (b) Schematic detail of the cap interface.

Key Research Accomplishments

1. We have developed and validated a rat model of temporal lobe epilepsy.
2. We have performed extensive *in vivo* experiments to achieve concurrent EEG and PAT recordings. Interesting results are obtained that may be significant for seizure prediction and for neurovascular coupling studies.
3. We have designed and constructed a light-weighted animal/transducer interface that can be used for chronic monitoring of freely moving animals.

Reportable Outcomes (see the Appendix to this Summary Report)

We have published two journal papers during Year 4. In addition, we expect that the results generated from the enormous amount of animal experiments to be completed in Year 5 will allow us to produce numerous journal publications and conference proceedings at the completion of this project.

Conclusions

The real-time PAT system constructed in this project coupled with the light-weighted cap interface has provided us a platform for performing extensive animal experiments in freely moving rats. In Year 5 we will complete the proposed Tasks 6 and 7 for continuous recording of EEG and PAT over a long period of time to monitor seizure activity continuously to characterize changes during interictal, ictal and post-ictal periods when a spontaneous seizure occurs. We will analyze the images from the *in vivo* experiments and write final reports. We will complete any unfinished experimentation during these months such that we have a sufficient number or

rats monitored with EEG and PAT to reach statistical significance. During this period, we will continue to evaluate our results and draft reports and manuscripts accordingly.

Appendix

(1) Bo Wang, Liangzhong Xiang, Max S. Jiang, Jianjun Yang, Qizhi Zhang, Paul R. Carney, and Huabei Jiang, Photoacoustic tomography system for noninvasive real-time three-dimensional imaging of epilepsy, *Biomed. Opt. Express* **3**, 1427-1432 (2012).

(2) L. Xiang, L. Ji, T. Zhang, B. Wang, J. Yang, Q. Zhang, M. S. Jiang, J. Zhou, P. R. Carney, H. Jiang, "Non-Invasive Real-Time Tomographic Imaging of Epileptic Foci and Networks," *NeuroImage* **66**, 240-248 (2013).

Photoacoustic tomography system for noninvasive real-time three-dimensional imaging of epilepsy

Bo Wang,¹ Liangzhong Xiang,¹ Max S. Jiang,¹ Jianjun Yang,¹ Qizhi Zhang,¹ Paul R. Carney,^{1,2,3,4,5} and Huabei Jiang^{1,*}

¹J. Crayton Pruitt Family Department of Biomedical Engineering, University of Florida, Gainesville, FL 32611, USA

²Department of Pediatrics, University of Florida, Gainesville, FL 32611, USA

³Neurology and Neuroscience, University of Florida, Gainesville, FL 32611, USA

⁴Wilder Center of Excellence for Epilepsy Research, University of Florida, Gainesville, FL 32611, USA

⁵McKnight Brain Institute, University of Florida, Gainesville, FL 32611, USA

*hjiang@bme.ufl.edu

Abstract: A real-time three-dimensional (3D) photoacoustic imaging system was developed for epilepsy imaging in small animals. The system is based on a spherical array containing 192 transducers with a 5 MHz central frequency. The signals from the 192 transducers are amplified by 16 homemade preamplifier boards with 26 dB and multiplexed into a 64 channel data acquisition system. It can record a complete set of 3D data at a frame rate of 3.3 f/s, and the spatial resolution is about 0.2 mm. Phantom experiments were conducted to demonstrate the high imaging quality and real time imaging ability of the system. Finally, we tested the system on an acute epilepsy rat model, and the induced seizure focus was successfully detected using this system.

© 2012 Optical Society of America

OCIS codes: (110.5120) Photoacoustic imaging; (170.6920) Time-resolved imaging.

References and links

1. R. A. Kruger, R. B. Lam, D. R. Reinecke, S. P. Del Rio, and R. P. Doyle, "Photoacoustic angiography of the breast," *Med. Phys.* **37**(11), 6096–6100 (2010).
2. A. A. Karabutov, E. Savateeva, and A. Oraevsky, "Imaging of layered structures in biological tissues with photoacoustic front surface transducer," *Proc. SPIE* **3601**, 284–295 (1999).
3. J. Xiao, L. Yao, Y. Sun, E. S. Sobel, J. He, and H. Jiang, "Quantitative two-dimensional photoacoustic tomography of osteoarthritis in the finger joints," *Opt. Express* **18**(14), 14359–14365 (2010).
4. X. Wang, Y. Pang, G. Ku, G. Stoica, and L. V. Wang, "Three-dimensional laser-induced photoacoustic tomography of mouse brain with the skin and skull intact," *Opt. Lett.* **28**(19), 1739–1741 (2003).
5. Q. Zhang, Z. Liu, P. R. Carney, Z. Yuan, H. Chen, S. N. Roper, and H. Jiang, "Non-invasive imaging of epileptic seizures in vivo using photoacoustic tomography," *Phys. Med. Biol.* **53**(7), 1921–1931 (2008).
6. J. Gamelin, A. Maurudis, A. Aguirre, F. Huang, P. Guo, L. V. Wang, and Q. Zhu, "A real-time photoacoustic tomography system for small animals," *Opt. Express* **17**(13), 10489–10498 (2009).
7. D. W. Yang, D. Xing, S. H. Yang, and L. Z. Xiang, "Fast full-view photoacoustic imaging by combined scanning with a linear transducer array," *Opt. Express* **15**(23), 15566–15575 (2007).
8. S. Manohar, A. Kharine, J. C. G. van Hespren, W. Steenbergen, and T. G. van Leeuwen, "Photoacoustic mammography laboratory prototype: imaging of breast tissue phantoms," *J. Biomed. Opt.* **9**(6), 1172–1181 (2004).
9. T. N. Erpelding, Y. Wang, L. Jankovic, Z. Guo, J. Robert, G. David, C. Kim, and L. V. Wang, "Three-dimensional photoacoustic imaging with a clinical two-dimensional matrix ultrasound transducer," *Proc. SPIE* **7899**, 78990A, 78990A-6 (2011).
10. M. B. Roumeliotis, I. Kosik, and J. J. L. Carson, "3D photoacoustic imaging using staring, sparse array with 60 transducers," *Proc. SPIE* **8223**, 82233F, 82233F-6 (2012).
11. C. G. A. Hoelen and F. F. M. de Mul, "Image reconstruction for photoacoustic scanning of tissue structures," *Appl. Opt.* **39**(31), 5872–5883 (2000).
12. L. Yao and H. Jiang, "Photoacoustic image reconstruction from few-detector and limited-angle data," *Biomed. Opt. Express* **2**(9), 2649–2654 (2011).
13. L. Yao and H. Jiang, "Enhancing finite element-based photoacoustic tomography using total variation minimization," *Appl. Opt.* **50**(25), 5031–5041 (2011).

1. Introduction

Photoacoustic tomography (PAT) is a hybrid method that is capable of imaging optical absorption of tissue through the detection of ultrasound waves generated by a short laser pulse due to transient thermoelastic expansion. It has an imaging resolution that is superior to pure optical imaging at centimeter scale depths. To date PAT has been applied to the detection of breast cancer, skin cancer and osteoarthritis in humans [1–3], and functional brain imaging in small animals [4,5].

For small animal brain imaging, most prior PAT studies were mostly based on a single-transducer scanning system or a circular or linear array of transducers for only 2D imaging [5–7], and the scanning in z direction is needed for 3D imaging purpose, which leads to a non-optimal elevational resolution in the z direction. 2D planar array of transducers has recently been employed for 3D PAT imaging [8,9]. However, due to the limited aperture of 2D planar array transducers, features with high aspect ratio or with orientations oblique to the transducer surface suffer from distortion, and the azimuthal resolution is reduced. Thus, 2D planar array of transducers is not suitable for small animal brain imaging.

Compared to a 2D planar array, a spherical array can offer more complete angular views of the object, providing both high resolution and accurate feature definition regardless of shape or location of the object. The use of sparse spherical arrays for 3D PAT imaging has been recently reported [1,10], but due to the insufficient number of transducers used, these arrays were not designed for small animal brain imaging. The goal of this work is to present a sparse spherical array based PAT system that is specifically designed for real time 3D imaging of small animal brains. The work is a natural extension/improvement of our previous work which reported for the first time 2D PAT imaging of epileptic focus in small animals [5]. The current PAT system is based on a 2D spherical array of 196 transducers coupled with parallel data acquisition, offering a temporal resolution of 0.33 s for data acquisition. We demonstrate this system using static/dynamic phantom and *in vivo* animal experiments. To the best of our knowledge, this is the first work reporting 3D PAT imaging of epileptic focus in small animals.

2. System descriptions

Figure 1 depicts the block diagram of our real-time 3D PAT system. A Ti:sapphire laser optically pumped with a Q-switched Nd:YAG laser sent 8–12 ns pulses at 10 Hz with a wavelength tunable from 690 to 1015 nm. The beam was delivered with an optical fiber

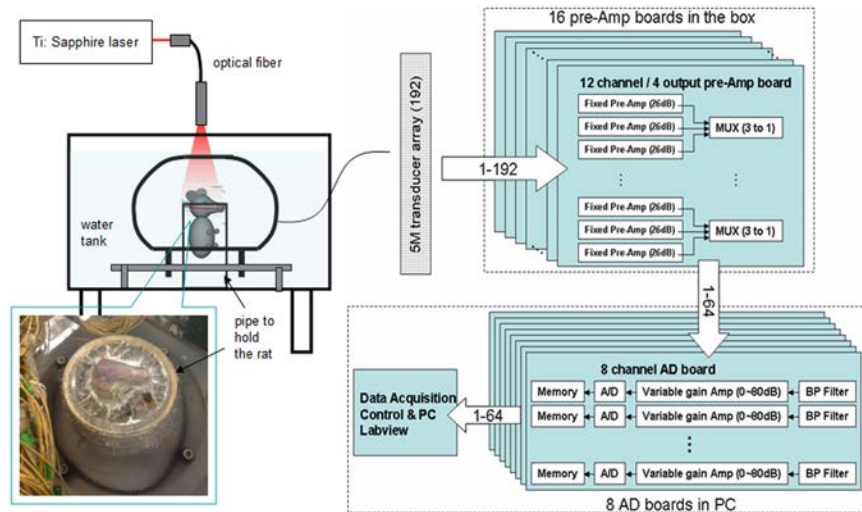


Fig. 1. Block diagram of our real-time 3D PAT system. The inset is a photograph of the close-up view of the chamber holding the rat head.

through an opening on the top of the transducer array and produced an approximately uniform illumination in a 2cm-diameter area onto the sample.

The transducer array consisted of 192 transducers placed along a custom fabricated white ABS spherical interface containing 610 through holes with counter bores, as shown in Fig. 2(a). More holes were drilled so that the selection of the transducer positions on the ball can be flexible. The interface has an outer diameter of 160 mm and an inner diameter of 140 mm, and the diameter of the holes in the ball is 5.7 mm, which fitted well with the transducer (5.5 mm outer diameter). Each transducer (Custom designed from Blatek, Inc.) has a central frequency of 5 MHz with a reception bandwidth of greater than 80%. The active area of the transducer is 3 mm in diameter and the angular acceptance is about 15 degree. The transducers were glued onto the interface with epoxy which can be removed to allow the position change of the transducers.

There were 16 preamplifier boards separately sealed in 4 metal boxes, and each board had 12 input channels, 4 output channels, and 2 digital signal control inputs. Within each board, 12 dedicated operational amplifier modules (AD8099) individually amplify the input signals with a fixed gain of 26 dB, and then the amplified signals were multiplexed into the 4 output channels by 4 multiplexer chips (MAX 4051), which were controlled by a USB IO digital module (USB-1024LS, Measurement Computing) through the 2 digital inputs.

The 64-channel parallel data acquisition system consisted of eight 8-channel PCI cards (PCIAD850, US Ultratek) in an industrial computer. For each channel, 3000 sampling points were collected at 50 MHz sampling rate in 10 bits, and stored in a 32k on board memory before they were transferred to the host machine. Amplifiers with a programmable gain of 0 to 80 dB along with a 16 MHz low band pass filter were built into the data acquisition system. A Labview program controlled the data acquisition, and the acquired data was stored on hard disk for further image processing. Images were reconstructed with a delay-and-sum algorithm [11]. For 3D image display, the reconstructed results were normalized to 0~255 after setting the negative values to be zero. Then 3D images were rendered with Amira (from Visage Imaging, Inc.) with different thresholds as indicated in the colorbar shown in each image.

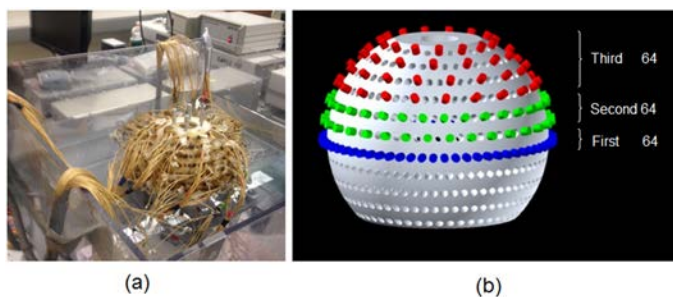


Fig. 2. The spherical transducer array. (a) Photograph of the transducer array. (b) 3D schematic of the transducer distribution on the interface.

The system allows the selection of transducer positions on the spherical interface. The total 610 holes formed 11 evenly spaced layers along the vertical direction of the ball, and the 192 transducer positions were indicated with three different colors in Fig. 2b. Three different colors were used to indicate the 3 to 1 multiplexing from the 192 transducers to the 64-channel data acquisition. This system can also be used as a real-time 2D system operating at 10 f/s using the 64 transducers arranged in the vertical center layer (blue). For *in vivo* experiments, the rat head was elevated to the center of the spherical interface through a chamber fixed at the tank bottom, whose top was about 15 mm beneath the interface center, and a transparent plastic wrap was used to cover the chamber top. For phantom experiments, a homemade silicone holder was used to hold the phantom.

3. Phantom experiments

Three different types of phantoms were used: One containing a point object for system calibration, one phantom containing three hairs tilted along different orientations for static imaging, and one phantom with ink flowing through a thin tube embedded in a phantom for real-time 3D imaging.

The point object used for calibration was a small spherical graphite particle (0.1 mm in diameter) located at the center of the spherical array and ensured an isotropic acoustic emission profile for all directions. We measured and compensated the delay of time for all the 192 channels in the radial direction, and reconstructed this point object after calibration. The hairs-containing phantom was used to demonstrate the high imaging quality of our system. Finally, we imaged an embedded tube filled with flowing ink to show the real-time imaging ability of our system. The tube had a 0.3 mm inner diameter and was horizontally placed in a phantom. No averaging of signals was performed for the phantom experiments except for the point object experiment where 10 times averaging was applied.

3.1. System characterization

We calibrated the system by recording the emission profiles from the spherical graphite particle for all the 192 channels, and then measured and compensated the time delay of each channel. We then evaluated the system resolution by reconstructing the image of the point object.

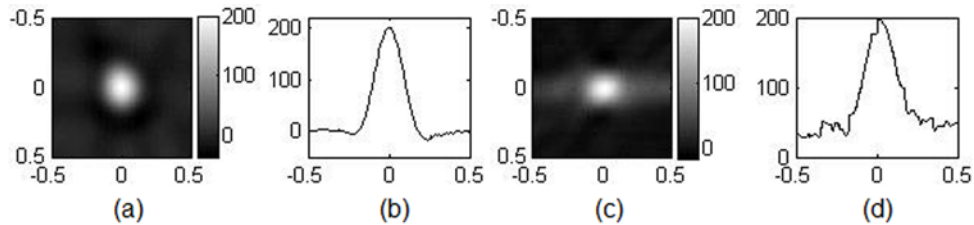


Fig. 3. (a) and (c): x-y and z-x cross section images through the center plan of the point object. (b) and (d): the profile extracted in x and z directions from (a) and (c), respectively. Units are in mm.

Figures 3a and 3c present the reconstructed x-y and z-x cross-section images of the point object located at the array center. The quality of these images is determined by both the distribution and the characteristics of the transducers. The profiles of the two reconstructed images were also extracted in x and z directions, as shown in Figs. 3b and 3d, respectively. The full width at half maximum (FWHM) of the profiles was measured to be 0.19 mm (x direction) for Fig. 3b, and 0.27 mm (z direction) for Fig. 3d, compared to the theoretical value of 0.16 mm for the 5 MHz central frequency transducer with an estimated cut off frequency of 7 MHz. It is noted that the profile in Fig. 3d is noisier than that in Fig. 3b. This along with a larger FWHM from Fig. 3d was due to the asymmetric distribution of the transducers. For targets located away from the center of the array, the radial resolution will stay nearly the same as that for a centrally located target, while the lateral resolution will be linearly reduced with increased distance away from the array center. In our system, the lateral resolution will be reduced by 0.1 mm when the target is located 5 mm off the array center.

3.2. Static phantom experiments

Figure 4a is the photograph of the phantom containing three hairs tilted along different orientations, and Figs. 4b and 4c show the reconstructed 3D images from two different views. The reconstructed volume is 10 x 10 x 10 mm with a 0.1 mm voxel size. The spatial distribution and tails for all the three hairs were clearly revealed. This result indicates that our system is capable of three-dimensionally imaging small objects of different spatial distribution and orientation in high quality.

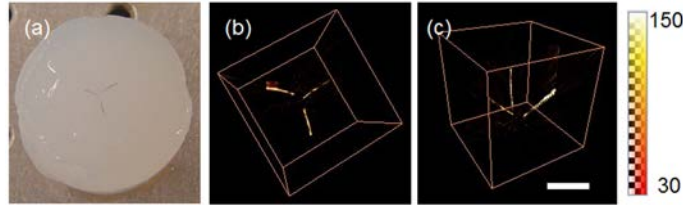


Fig. 4. (a): photograph of the phantom containing three tiled hairs; (b)-(c): reconstructed 3D images of the three hairs in two different views. Scale bar represents 5 mm.

3.3. Dynamic phantom experiments

The reconstructed 3D images of ink flowing through a thin tube are shown in Fig. 5. The image domain is 15 x 5 x 10 mm with a 0.1 mm voxel size. Figure 5a is the photograph of the phantom containing a tube filled with ink, and Figs. 5b–5j are the reconstructed 3D images at different time points. The time interval between two consecutive images was 0.3 s. These 3D images clearly tracked the flow through the tube over the course of 2.4 seconds with high spatial and temporal resolution, and the flowing speed of the ink was measured to be 6 ± 0.9 mm/s from the reconstructed results with a time interval of 0.3 s.

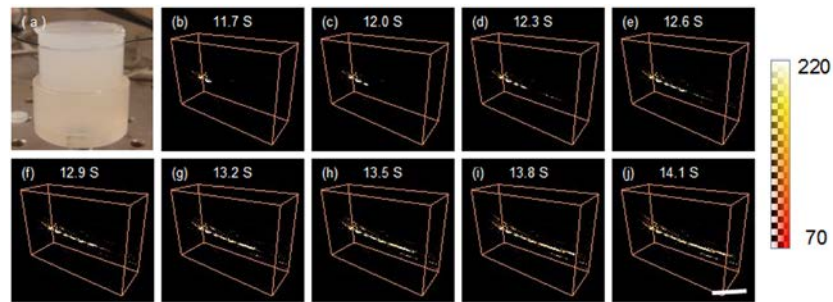


Fig. 5. Reconstructed 3D images of ink flowing through a 0.3 mm-tube embedded in a background phantom. (a): photograph of the phantom containing the tube. (b)-(j): reconstructed 3D images at different time points. The time interval is 0.3 s. Scale bar represents 5 mm.

4. Rat epilepsy experiment

Epilepsy is a serious brain disorder involving intensive hemodynamic changes, which provides high endogenous contrast for PAT imaging due to the strong absorption of blood at visible and NIR wavelengths. Compared with current existing neuron-imaging methods (such as MRI, CT, PET, and SPECT), PAT provides not only high ultrasound resolution and high optical contrast, but also unprecedented advantage of high temporal resolution over these methods, which is critical for capturing seizure dynamics.

2D PAT of seizure focus on an acute seizure rat model was demonstrated for the first time by our lab [5], but the observation of hemodynamic changes during seizure onset was hindered by the long time scanning of a single transducer. Here we test our real-time 3D system using the same animal model to show the hemodynamic changes and reveal the 3D structures in the rat brain.

Two small rats (~40g) were imaged with intact skull and skin but hairs on the head were removed. The rats were anaesthetized and mounted on the homemade plastic chamber/holder. Focal seizure was induced by microinjection of 10 μ l of 1.9 mM bicuculline methiodide (BMI) into the neocortex of one rat, while saline solution was injected into the brain of another rat as control. In each experiment, the rat was elevated to the transducer array center and kept alive under the water tank through the whole experiment. The incident energy of the 730 nm light was maintained at 8mJ/cm² below the safety standard. Seizure process was recorded for 50 minutes, and the measurement from the control rat was recorded for 3 s. All

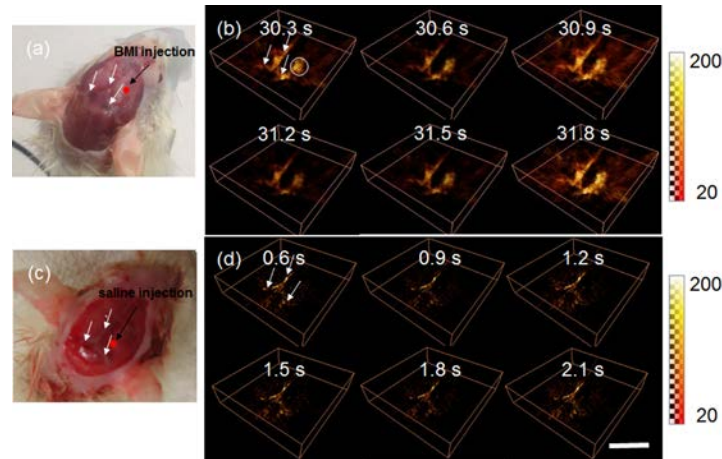


Fig. 6. (a) and (c): photograph of the rat with BMI injection and the control rat after scalp removed. (b) and (d): 3D PAT images at 6 time points for (a) and (c) respectively. The three main blood vessels are indicated by the white arrows, and the seizure focus is indicated by the circle in (b). The time interval between two successive images is 0.3 s. Scale bar represents 10 mm.

animal procedures were performed in accordance with the approved University of Florida IACUC protocols.

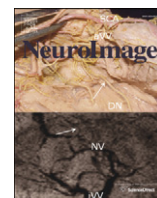
Figure 6b presents the 3D images for the rat with BMI injection during the seizure onset at 6 time points, compared with that for the control rat in Fig. 6d. The corresponding photographs of the two rats with scalp removed right after the experiments are shown in Figs. 6a and 6c, respectively. The reconstructed domain for the images shown in both Figs. 6b and 6d is $20 \times 20 \times 4.5$ mm, with a 0.1 mm pixel size. The three main blood vessels on the rat brain are clearly revealed for both cases, as indicated by the white arrows, and for the rat with BMI injection a seizure focus can be clearly seen right at the BMI injection position (the white circle in Fig. 6b), where strong absorption is observed during seizure onset. The rapid changes of the absorption both in the main blood vessel and in the seizure focus were observed from Fig. 6b, while no such changes were noted for the control rat (Fig. 6c). The seizure focus had a diameter of ~ 3 mm, which is consistent with the results published before [5]. This experiment demonstrates that our system can be used to investigate the hemodynamic changes in small animal brain both spatially and temporally during seizure onset, although the complex microvasculature cannot be resolved due to the limited number of transducers and the simple backprojection reconstruction method used here. The microvasculature can be revealed if sophisticated reconstruction methods such as the finite element based algorithms coupled with the total variation minimization scheme are used [12,13].

5 Conclusions

We have presented a real-time photoacoustic system for three-dimensionally imaging focal cortical seizures in a rat. The system is based on a spherical array containing 192 discrete transducers. With the 64-channel data acquisition system coupled with 3:1 multiplexing, it can achieve a frame rate of 3.3 f/s with a spatial resolution of 0.2 mm. The 3D imaging performance of the system was demonstrated by both static and dynamic phantom experiments. We have also tested our system using an acute epilepsy rat model and obtained 3D images showing the hemodynamic changes during seizure onset.

Acknowledgments

This research was supported in part by a grant from the U.S. Department of Defense Congressionally Directed Medical Program, the B.J. and Eve Wilder endowment fund, and the Children's Miracle Network.



Noninvasive real time tomographic imaging of epileptic foci and networks

Liangzhong Xiang^a, Lijun Ji^a, Tao Zhang^a, Bo Wang^a, Jianjun Yang^a, Qizhi Zhang^a, Max S. Jiang^a, Junli Zhou^{b,c}, Paul R. Carney^{a,b,c,d}, Huabei Jiang^{a,*}

^a J. Crayton Pruitt Family Department of Biomedical Engineering, University of Florida, Gainesville, FL 32611, USA

^b Departments of Pediatrics, Neurology, and Neuroscience, University of Florida, Gainesville, FL 32611, USA

^c Wilder Center of Excellence for Epilepsy Research, University of Florida, Gainesville, FL 32611, USA

^d McKnight Brain Institute, University of Florida, Gainesville, FL 32611, USA

ARTICLE INFO

Article history:

Accepted 25 October 2012

Available online 2 November 2012

Keywords:

Real time photoacoustic tomography (PAT)

Noninvasive seizure dynamic imaging

Epileptic foci and networks

Pre-surgical planning

ABSTRACT

While brain imaging and electrophysiology play a central role in neuroscience research and in the evaluation of neurological disorders, a single noninvasive modality that offers both high spatial and temporal resolution is currently not available. Here we show in an acute epilepsy rat model that photoacoustic tomography (PAT) can noninvasively track seizure brain dynamics with both high spatial and temporal resolution, and at a depth that is clinically relevant. The noninvasive yet whole surface and depth capabilities of the PAT system allowed us to actually see what is happening during ictogenesis in terms of seizure onset and spread. Both seizure onset and propagation were tomographically detected at a spatial resolution of 150 μm and a temporal resolution of 300 ms, respectively. The current study lends support to the theory that seizure onset and spread involves a rich interplay between multiple cortical and subcortical brain areas during the onset and spread of epileptic seizures. Dynamical changes of vasculature during epileptiform events were also detected with high spatiotemporal resolution. Together, these findings suggest that PAT represents a powerful tool for noninvasively mapping seizure onset and propagation patterns, and the 'functional' connectivity within epileptic brain networks.

© 2012 Elsevier Inc. All rights reserved.

Introduction

Epilepsy is a common, chronic, neurological disorder characterized by seizures. Three percent of people will be diagnosed with epilepsy at some time in their lives (Hauser et al., 1996). Indeed, approximately 50 million people worldwide have epilepsy, and 20 to 30% of these patients are refractory to all forms of medical treatment (Hauser, 1992). In most cases, seizures are controlled, although not cured, with anticonvulsant medication. Seizure types are classified according to whether the source of the seizure is localized (partial or focal onset seizures) or distributed (generalized seizures) (Greenfield et al., 2011). Localization-related epilepsies arise from an epileptic focus. A partial seizure may spread within the brain, a process known as secondary generalization. Generalized epilepsies, in contrast, arise from many independent foci (multifocal epilepsies) or from epileptic circuits that involve the whole brain. In epilepsies of unknown localization, it remains unclear as to whether they arise from a portion of the brain or from more widespread circuits.

For those patients with medically intractable focal epilepsy, the best treatment option is resective brain surgery (Berg et al., 2007; Birbeck et al., 2002; Duncan et al., 2006). Although several factors can impact the success of epilepsy surgery, the primary reason of failure is the incomplete mapping of the local epilepsy network which results in incomplete resection of epileptogenic foci (Engel, 2004; Jeha et al., 2007). Much of the attention on epilepsy surgery has been directed at identifying single neuronal populations. This approach has, in many cases, led to failed surgical outcomes, because seizures typically involve groups of neurons interacting both locally and across several cortical and subcortical brain regions. A better understanding of the regional interactions occurring at the site of seizure onset and spread may provide important insights about the pathophysiology of seizures and aid with accurate brain mapping and resection of the epileptic focus.

In theory, removing the focus should result in a patient's seizures being cured. However, there is much evidence to suggest that the focus is more of a region of seizure onset with a number of sites that can act independently to initiate seizures (Thom et al., 2010a, b). Seizures in animal models and in people often have a multifocal or broadly synchronized onset. The best evidence for multifocality within the seizure onset zone comes from surgical experience with intracranial monitoring. The challenge of mapping the epileptic focus stems from the observation that the pathology associated with focal epilepsy is often distributed across a number of brain sites

* Corresponding author at: University of Florida College of Engineering, J. Crayton Pruitt Family Department of Biomedical Engineering, JG56 BMS Building, Gainesville, FL 32611, USA.

E-mail address: hjiang@bme.ufl.edu (H. Jiang).

(Bertram, 2009) and that current diagnostics methods frequently fall short of identifying such sites. Animal studies indicate that the neurons involved in the epileptic circuitry have enhanced excitability throughout (Bertram et al., 1998; Fountain et al., 1998; Mangan et al., 2000). The implication of these observations is that each of the sites could act independently to initiate a seizure or, potentially, to drive another site into a seizure. Thus, in focal epilepsy, one may view a cortical region as a broad seizure onset zone, with the potential that multiple foci can act as a seizure focus for any given seizure.

Much of our understanding about focal seizure circuitry comes from electrophysiological recording methods. Although electrophysiology is currently the ‘gold standard’ in mapping the epileptic focus, it is often inadequate to define the boundary of the epilepsy circuitry due to spatial sampling limitations and volume conduction. What we truly desire is a brain mapping modality, which could give a high-resolution real time spatial and temporal ‘read out’ of the dynamics of cortical processing and seizures. It has been well established that optical contrast is highly sensitive to neuronal activity (Grinvald et al., 1988; Hill and Keynes, 1949). The high optical contrast is largely due to the changes in blood volume and blood oxygenation, both of which substantially increase during seizures, and increase in oxygenation metabolic rate results in increased demands on autoregulatory mechanisms (Folbergrová et al., 1981). Taking the advantage of the oxygenation dependence in the optical absorption spectrum of hemoglobin, optical imaging or intrinsic optical signal (IOS) methodologies have provided excellent surface maps of epileptic focus (Haglund and Hochman, 2004; Haglund et al., 1992). Although near-infrared spectroscopy (NIRS) (Steinhoff et al., 1996; Sokol et al., 2000; Watanabe et al., 2000) and blood-oxygen-level-dependent (BOLD) MRI can assess oxygen saturation with endogenous contrasts, BOLD MRI is sensitive only to HbR with low temporal resolution (Ogawa et al., 1990). In addition, the major limitation of NIRS and IOS is that each provides only surface depth information. Greater depth information can be obtained by using tomographic reconstruction methods such as diffuse optical tomography (Bluestone et al., 2001; Boas et al., 2001; Jiang et al., 1996; O’Leary et al., 1995). Whereas diffuse optical tomography has low spatial resolution, laser-induced photoacoustic tomography (PAT) has both superior spatial and temporal resolution. PAT detects absorbed photons ultrasonically by employing the photoacoustic effect. It combines both high contrast and spectroscopic specificity based on the optical absorption of both oxy- and deoxy-hemoglobin with high ultrasonic spatial resolution (Kruger and Liu, 1994; Laufer et al., 2007; Xiang et al., 2007; Yuan et al., 2007). Relative to other optical imaging modalities, PAT has the advantage of mitigating both scalp and skull light scattering by a factor of ~1000. The end result is that PAT allows for high spatial resolution imaging of brain at a depth considerably beyond the soft depth limit of conventional optical imaging techniques such as confocal microscopy (Sipkins et al., 2005), two-photon microscopy (Denk et al., 1990), and optical coherence tomography (Huang et al., 1991). The strong preferential optical absorption of hemoglobin makes PA imaging to have a better imaging contrast than ultrasound (US); as it can be difficult to visualize the microvessels with pulse-echo US owing to the weak echogenicity (Mace et al., 2011).

In this study, PAT was employed to image seizures in an experimental acute bicuculline methiodide model of focal epilepsy. Bicuculline is a light-sensitive competitive antagonist of GABA_A receptors that mimics focal epilepsy when applied to brain tissue. During focal application of bicuculline into the brain cortex, brains were imaged noninvasively with a novel PAT system that has three orders of magnitude higher temporal resolution and four-fold higher spatial resolution relative to our previous PAT prototype (Zhang et al., 2008). Off-line, we employed measures of brain connectivity to further identify the functional anatomy implicated in focal cortical seizures. The high spatial and temporal sampling of the novel PAT system allowed for the first time the complete mapping of an epileptiform event *in vivo*.

Methods

Animals

Male Sprague–Dawley rats (Harlan Labs, Indianapolis, IN) weighing 50–60 g on arrival were allowed one week to acclimate to the 12-h light/dark cycle and given food and water ad libitum. All procedures were approved by the University of Florida Animal Care and Use Committee and conducted in accordance with the National Institutes of Health Guide for the Care and Use of Experimental Animals.

PAT imaging

Light from a Ti: Sapphire laser tunable (690 to 950 nm) was delivered through the skull to the brain through an optical fiber (Fig. 1a). The energy of each laser pulse was detected by a photodiode for calibration. A 192 element full-ring transducer array was used to capture the photoacoustic (PA) signals generated by the laser light. The 192 channel data acquisition system consisted of preamplifiers, secondary stage amplifiers (for optimizing the signal-to-noise ratio), and a 3:1 electronic multiplexer coupled with a 64-channel analog-to-digital converter. Each ultrasonic detector had a 5-MHz central frequency and a 70% nominal bandwidth with a diameter of 6 mm (Blatek, Inc., PA, USA).

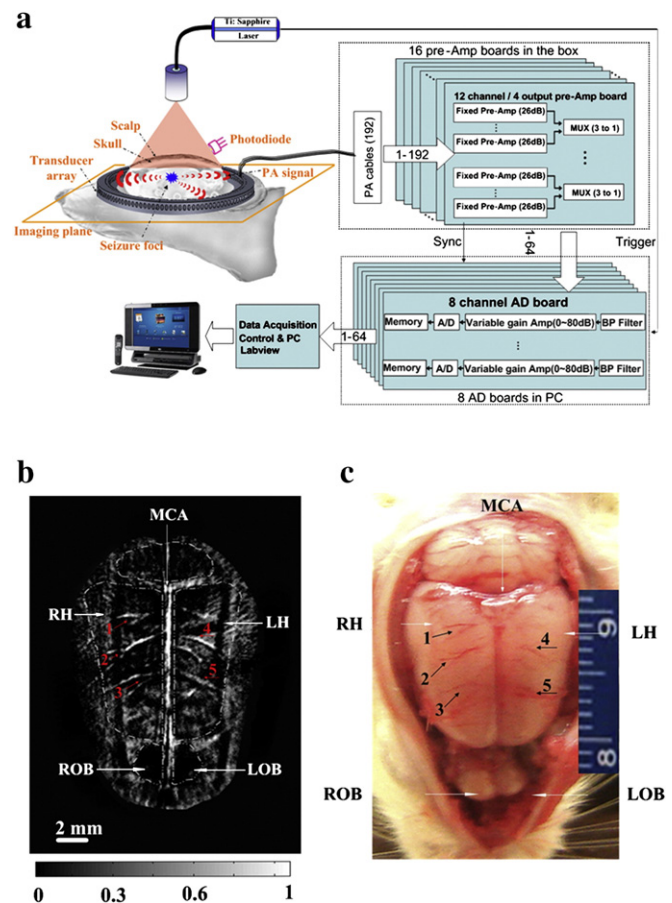


Fig. 1. Real time PAT system for seizure dynamics. (a.) Schematic of the real time PAT system. A 192-element full-ring transducer array was used to capture the PA signal during seizure onset. (b.) Noninvasive PAT imaging of a rat brain *in vivo* with the skin and skull intact. MCA, middle cerebral artery; RH, right hemispheres; LH, left hemispheres; LOB, left olfactory bulbs; ROB, Right olfactory bulbs. (c.) Open-skull photograph of the rat brain surface acquired after the PAT experiment. Numbers 1–5 indicate the corresponding blood vessels in the PAT image and rat brain photograph.

Electrode implantation surgery

Animals were anesthetized intraperitoneally with 1 g/kg of body weight dose of urethane. Two 300 μm diameter stainless steel screw electrodes were implanted within the skull for obtaining subdural multichannel cortical local field potentials data (-0.3 mm posterior, 3 mm lateral (right) of bregma, 1 mm ventral) based on coordinates from a rat brain atlas (Paxinos, 1998). One, 300 μm diameter stainless steel screw electrode (FHC, Bowdoin, ME) was implanted as a reference electrode into the midline occipital bone. Cortical local field potentials were obtained using a Tucker Davis Pentusa (Tucker Davis Technologies, Alachua, FL) neural recording system at 12 kHz, digitized with 16 bits of resolution, and band pass filtered from 0.5 to 6 kHz.

Induction of seizures

Rats ($n=10$) received 10 μl of 1.9 mM bicuculline methiodide and 10 μl normal saline into the left and right parietal cortex, respectively. The infusion was performed through the previously implanted electrode sites at a rate of 0.3 $\mu\text{l}/\text{min}$. The infusion system consisted of a 100 μl gas-tight syringe (Hamilton, Reno, NV) driven by a syringe pump (Cole-Parmer, Vernon Hills, IL) connected to polyaryletheretherketone (PEEK) tubing (ID = 0.381 mm, OD = 0.794 mm, length ~ 0.5 m, Upchurch Scientific, Oak Harbor, WA). The PEEK tubing was coupled to a silica cannula (ID = 50 μm , OD = 147 μm , Polymicro Technologies, Phoenix, AZ) via a microfluidic connector. Cortical local field potentials were recorded 5 min before each injection and continued for up to 30 min thereafter.

Image analysis

A custom software utility was written and incorporated into the computer software package MATLAB (MathWorks, Massachusetts, USA) to analyze and display recorded data. This software enabled the reconstruction of the PAT images and the determination of the blood vessel diameter. Amira (version 5.3.3, TGS Template Graphics Software) was used for three-dimensional reconstruction of the seizure foci. We used the frequency domain Granger causality methodology to evaluate the dynamic interactions within the seizure circuitry and the associated brain networks (Brovelli et al., 2004; Granger, 1969; Wang et al., 2007). The time-series data were selected from 200 sets of PAT images sampled at 3 Hz within the seizure onset period, and at each time point, we chose 9 (regions of interest) ROI (R1–R9) and then the PA signal was averaged within each ROI, as shown in Fig. 5b1. Changes in photoacoustic signals were quantified as $-\Delta A/A$ in Fig. 5b3, right. The PA data shown in Figs. 3–5 were not averaged. The image color scale was determined by the photoacoustic signal intensity in arbitrary units (between 0 and 1).

Results

Noninvasive epileptic foci localization

Temporal and spatial resolutions of the PAT system were experimentally determined. PA images depicting frames from a 10-second sequence of dynamic ink flow through a 0.3 mm diameter tube was shown in Movie S1. The movie shows that the temporal resolution of this imaging system was ~ 0.33 s/frame. Cross-sectional PA image of a two-copper-rods phantom was used to test the spatial resolution of the PAT imaging system. The two copper rods (diameter: 0.05 mm) were embedded in a cylindrical tissue-mimicking phantom at a depth of 10 mm. The center-to-center distance between the two copper rods was approximately 2.2 mm. The spatial resolution of the imaging system calculated with Rayleigh's law was 150 μm . The spatial

resolution of the PAT system was inversely related to the bandwidth of the ultrasonic transducer.

The noninvasive PAT image of the rat cortical vasculature (Fig. 1b) matched well with an anatomical atlas (Paxinos, 1998) (Fig. 1c) obtained after the PA imaging. The brain structures including the middle cerebral artery, right hemispheres, left hemispheres, left olfactory bulbs, and right olfactory bulbs are clearly shown in the PAT image. Numbers 1–5 marked in the image indicate that the micro-blood vessels with a diameter of less than 100 μm are also seen, which again correspond well with the rat brain photograph. This allowed for imaging objects of 50 μm in diameter with a spatial resolution of 150 μm (Figs. 2b, c).

Thirty minutes following the microelectrode placement, PAT imaging was performed to generate baseline tissue absorption maps, visualize micro blood vessels, and morphological cortical landmarks (Figs 3b, c). Subsequently, rats ($n=10$) received 10 μl of 1.9 mM bicuculline methiodide and 10 μl normal saline into the left [-1.0AP , 2.5ML, 2.4DV] and right [-1.0AP , 2.5 ML, 0.4DV] parietal cortex, respectively, based on coordinates from a rat brain atlas (Paxinos, 1998). Immediately following the focal infusions, PAT imaging was repeated to visualize changes in the injection site tissue absorption. An increase in tissue absorption was observed in the bicuculline methiodide cortical injection site and surrounding region (Fig. 3c, left), but not in the saline injection site or surrounding region (Fig. 3c, right). PAT scanning for subcortical changes was also performed. Slices 5, 7, and 9 (Fig. 3d) are the images obtained 3, 5 and 7 mm below the scalp, respectively. Fig. 3e is the three dimensional rendering of the epileptic foci obtained from different tomographic layers (movie S2). Each image exhibited the variable patterns of seizure onset and propagation both at the cortical and subcortical regions. Seizures were confirmed by concomitant time-locked PAT/video-electroencephalography (Fig. 3a). Experiments were repeated for each animal at 2-hour intervals.

Real time monitoring of epileptic events

Epileptiform events were recorded with PAT from a focal region of interest of $\sim 2 \times 3$ mm (Fig. 4a). We observed a significant optical absorption change directly associated with de-oxygenation at a wavelength of 755 nm (Fig. 4c). Furthermore, at the seizure onset at 1 min 6.267 s, the seizure focus measured 0.2053 mm^2 and increased to 0.5004 mm^2 as the electrographic seizure time-series increased in frequency and amplitude (Fig. 4b). Corresponding rate changes (0.33 s) spike and wave discharges and PA images were observed in each experimental trial. The seizure onset dynamics captured photoacoustically are best appreciated in movies displaying how the seizure was generated and varied over time (Movie S3). PAT images suggest that in addition to ictal spread from the primary focus, homotopic foci are seen in the contralateral parietal cortex (Fig. 5a1–4). The PA signal in the contralateral foci was smaller in magnitude and delayed in time compared to the signal recorded from the primary seizure foci. We also observed a region of inverted optical signal immediately surrounding the seizure onset zone (Fig. 5b2–3). We performed analysis of the optical signal at a distance of at least 2 mm (± 0.01) away from the edge of the focus. Our results demonstrate that the photoacoustic signal was inversely related to the optical signal recorded from the focus (Fig. 5b3).

To evaluate the dynamic interactions within the seizure circuitry and capture the associated networks we used the frequency domain Granger causality (Brovelli et al., 2004; Granger, 1969; Wang et al., 2007). PAT time series data was selected from 200 sets of PAT images sampled at 3 Hz within the seizure onset period. At each time point we chose 9 ROIs (Fig. 5b1) and used the averaged optical absorption within each region for the network analysis. Nine sets of time series analysis were classified into 3 groups including the primary ictal onset area and corresponding 4 surrounding regions of interest including the primary or initiating seizure focus, contralateral homotopic foci, and 2 regions of interest surrounding the primary focus in the

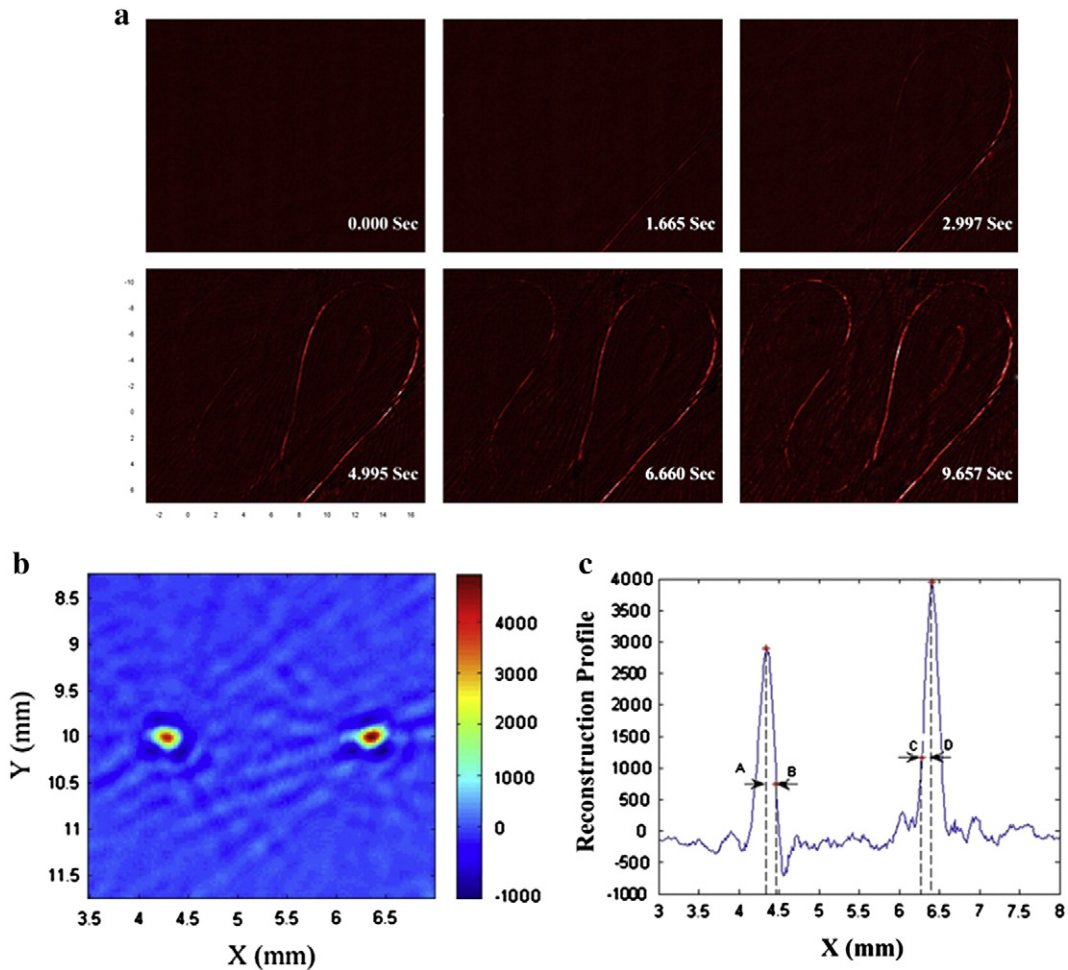


Fig. 2. Temporal and spatial resolution demonstration of the PAT system. (a.) Temporal resolution demonstration of the PAT system. Photoacoustic images depicting frames from a 10-second sequence of dynamic ink flow through a 0.3 mm diameter tube (Movie S1). The movie shows that the temporal resolution of this imaging system was ~ 0.33 s/frame. (b.) Cross-sectional PA image of a two-copper-rods phantom. The two copper rods (diameter: 0.05 mm) were embedded in a cylindrical tissue-mimicking phantom at a depth of 10 mm. The center-to-center distance between the two copper rods was approximately 2.2 mm. (c.) The normalized profile of the reconstructed PA image shown in (b.) along $y = 10$ mm. The half- and quarter-amplitude widths were obtained by measuring the distance between points AB and between CD, respectively. The spatial resolution of the imaging system calculated with Rayleigh's law was $150 \mu\text{m}$.

contralateral cortex. The middle cerebral artery, primary seizure focus, and secondary homotopic seizure focus were also analyzed. Results from group 1 analysis demonstrate the causal influence from the primary focus to the surrounding regions of interest (Fig. 5b1). The negative zero-lag correlation (-0.68) between both the primary and secondary foci showed that neural activities within these two regions changed in opposite direction over time. Fig. 5b4 shows the Granger causality analysis for group 2 data where we see that the primary and secondary contralateral brain foci influenced each other mutually with a stronger influence of the primary focus relative to the contralateral focus. Moreover, we suggest that the primary seizure focus may influence the contralateral foci as previously suggested using optical intrinsic imaging in epilepsy (Khalilov et al., 2003) and microelectrode recordings of hippocampus local field potentials (Cadotte et al., 2010). Finally, from group 3 analyses (Fig. 5b5) we found that the primary focus strongly influenced the hemodynamic change in the middle cerebral artery, which in turn showed influence on the contralateral homotopic foci.

Dynamical changes of vasculature during interictal discharges

Fig. 6a shows image of the rat cortex vasculature through the intact scalp and skull. The red arrow indicates the microvasculature along the direction marked by the yellow dashed line, representing a cross-sectional scanning using a 50 MHz ultrasound transducer. Positive and negative acoustic peaks induced by a $25 \mu\text{m}$ blood vessel

were sorted out as target signals to track the change of the vessel diameter. Typical PA signals from the targeted vessel at different times show apparent vessel vasomotion by $\sim 40\%$ (mean = 40%, $P < 0.03$, $N = 20$) during the interictal discharges (Fig. 6b). Local field potential recordings (Fig. 6c) showed that interictal spikes had a strong correlation with the discrete change in vessel size observed photoacoustically (Fig. 6d; error bars \pm s.d. was calculated from 20 consecutive spikes).

Discussion

The main finding is that PAT imaging is a novel tool for noninvasively mapping seizure dynamics with both high spatial and temporal resolution. This study investigated the hemodynamic changes during focal seizure onset and propagation in an acute model of focal epilepsy. The experimental results suggest that the increase in local and surrounding brain tissue absorption was due to the focal bicuculline methiodide induced seizure rather than other factors such as stab cortex tissue wound injection. Epileptiform events, including interictal spikes, ictal onset and spread were identified in near real time. To the best of our knowledge, this is the first experimental evidence for millisecond temporal resolution, centimeters depth, and micron scale imaging of focal seizure onset and spread by a noninvasive technique.

Quantitative photoacoustic image reconstruction can be used to resolve the light scattering problem with the deeper penetration in

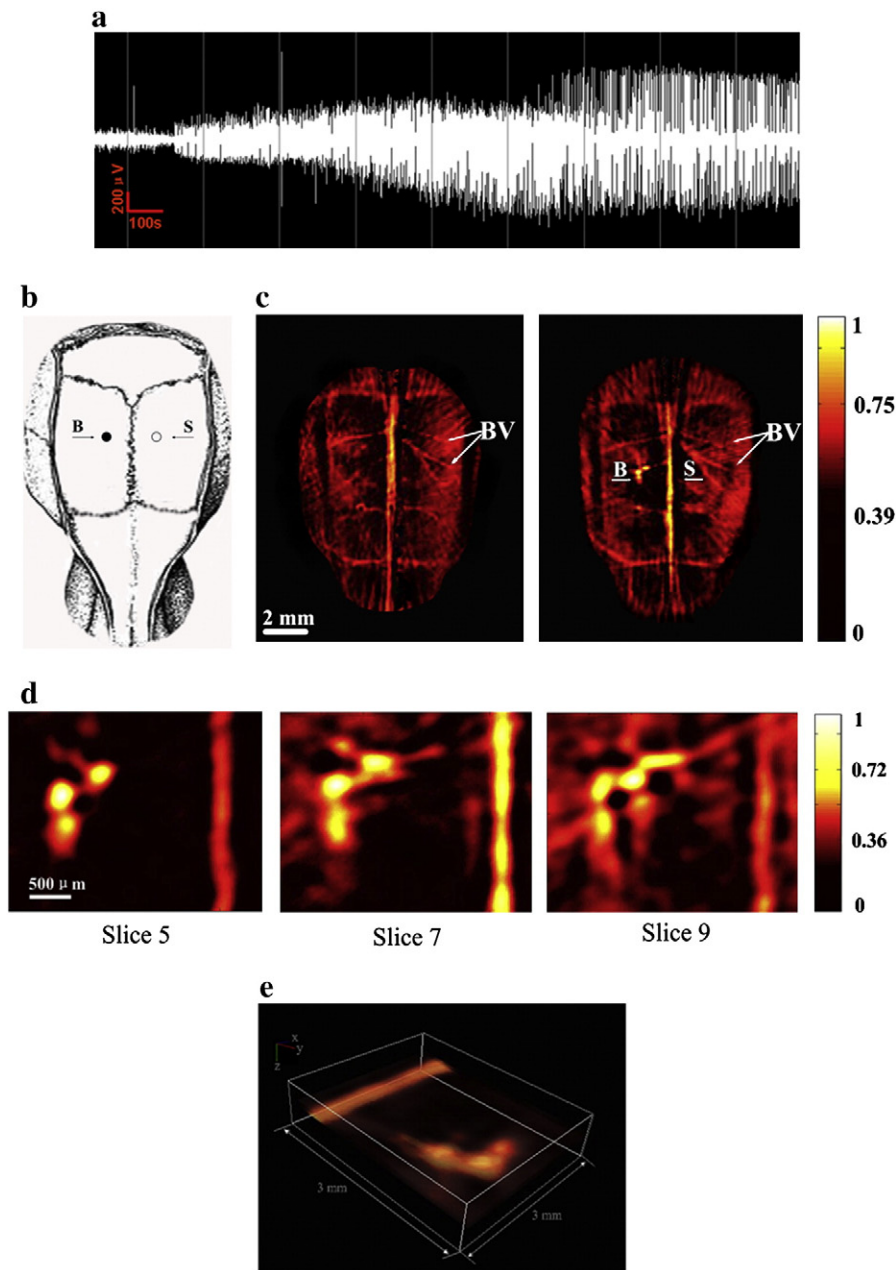


Fig. 3. Noninvasive epileptic foci localization. (a.) EEG recordings of seizure onset after BMI injection. (b.) Schematic showing the location of BMI injection and saline injection (control). B, BMI injection; S, saline injection. (c.) Reconstructed PAT image before (left) and after (right) the BMI injection. The BMI and saline were injected into the left and right parietal neocortex, respectively. A significant increase of optical absorption is seen in the region of the BMI injection, while no absorption contrast is observed in the region of the saline injection relative to its surroundings. (d.) Series of PAT images from three representative transverse planes parallel to the skin surface with 755 nm wavelength. Slices 5, 7, and 9 are the images obtained 3, 5 and 7 mm under the skin, respectively. The images show different spatial patterns at the seizure foci at different tomographic layers. (e.) Three dimensional rendering of the epileptic foci from different tomographic layers (Movie S2).

the tissue based on compensating the reconstructed image with a pre-calculated optical fluence distribution (Yao et al., 2009; Yuan et al., 2007). It is possible to achieve higher resolution at cellular and even sub-cellular levels to image the neuronal circuitry *in vivo* by use of photoacoustic microscopy at a depth of more than 3 mm (Shelton and Applegate; Hu et al., 2010). The findings imply that PAT has potential for noninvasive real time brain mapping of cortical processing and seizures.

A key advantage of our noninvasive PAT system for epileptiform event monitoring is the real time imaging ability. Seizures are generated by complex interactions of a large group of neurons in which the population of neurons involved varies largely from moment to moment (Schwartz and Bonhoeffer, 2001). By achieving 1000 times

faster data acquisition of the current PAT imaging system relative to our previous PAT system (Zhang et al., 2008), we were able to observe that the spatial aspects of the seizure focus varied over time as suggested by the changes in hemodynamics (Fig. 4c). At present, the imaging speed was limited only by the 10 Hz laser pulse-repetition-rate. Since considerably faster lasers of ~500 Hz pulse-repetition-rates are now commercially available, the temporal resolution of PAT will soon reach a level of a few milliseconds. The light fluence on the skin was less than 5 mJ/cm², well within the American National Standards Institute (Institute, 2007) safety limits. This, coupled with the compactness of an optical system makes it possible to bring a PAT system to the bedside for real time chronic noninvasive monitoring of seizures (Yang et al., 2007).

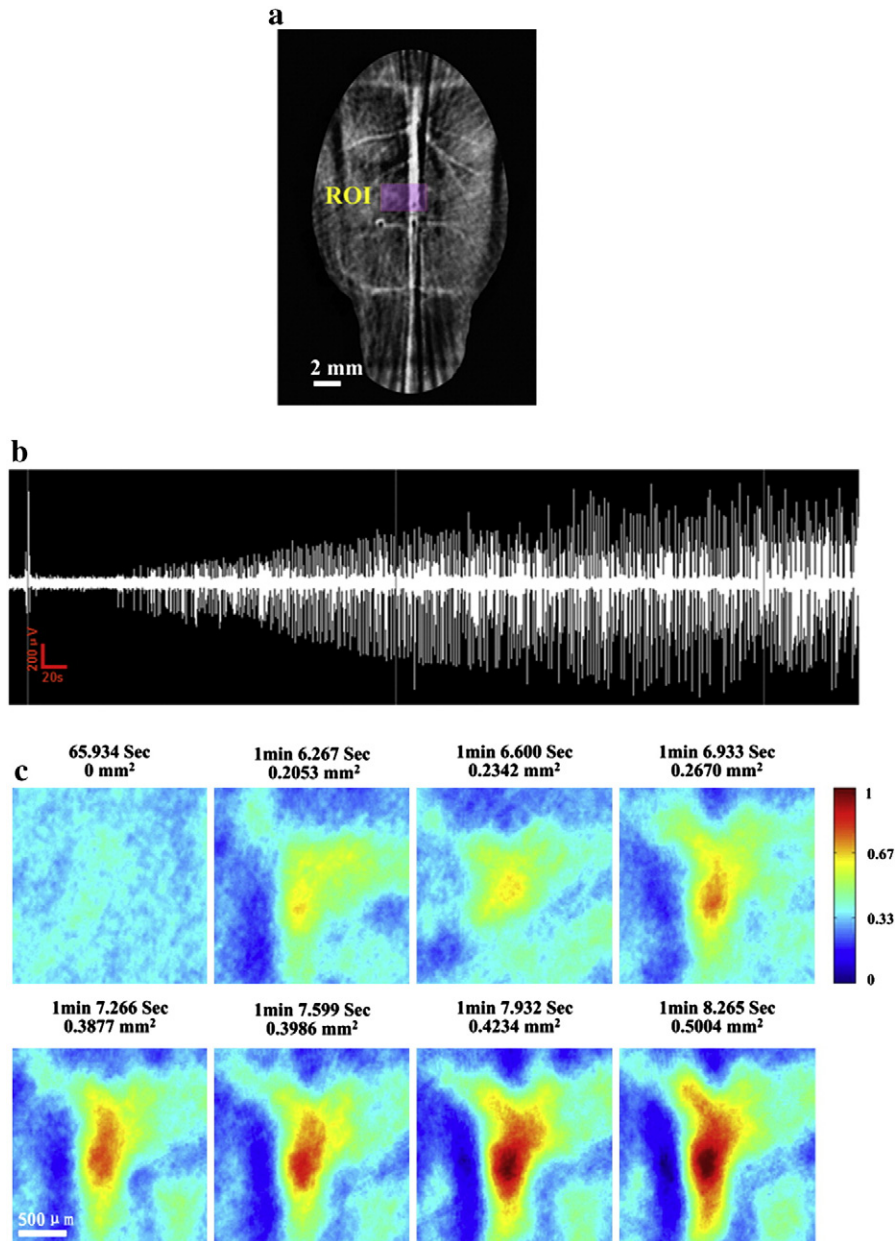


Fig. 4. Real-time monitoring of ictal onset. (a.) A PA image showing the cerebral vasculature and the position of BMI injection. ROI, region of interest; Scale bar: 2 mm. (b.) EEG recordings showing the seizure onset about 1 min after BMI injection. (c.) PAT images recording the ictal onset in real time. At 1 min 6.267 s the area of the focus was 0.2053 mm^2 . The area of the focus then increased in size over the next 2 s to 0.5004 mm^2 , corresponding to an increase in the amplitude of the EEG spikes. The area of the seizure focus was derived from the PAT images by thresholding to a pixel value one standard deviation above the pixel values from the area of the focus during the control conditions. Scale bar: $500 \mu\text{m}$ (Movie S3).

One hypothesis is that long-standing epilepsy may lead to the development of secondary epileptogenic regions located at a site distant from the original focus, a factor that may reduce the likelihood of successful epilepsy pre-surgical planning (Cendes et al., 1995). The ability to identify the epileptic focus and associated network may lead to better epilepsy surgery outcomes for many individuals. Various methods such as cross correlation and Granger causality have been explored for assessing the dynamic directional relationships among brain regions using time series data (Bressler et al., 2008; Kaminski et al., 2001). We used Granger causality as a way to quantify the dynamic interactions amongst the primary seizure focus, secondary seizure foci, and middle cerebral artery based on the time-series photoacoustic data. Specifically, Granger causality allowed for assessment of the magnitude and direction of temporal relationships during

overlapping PAT time-series windows. Results further exemplified the temporal aspects of seizure onset, seizure secondary spread, and seizure termination. Collectively, PAT image analysis and tools for effective connectivity may result in a better understanding of epileptic networks at high spatiotemporal resolution.

Little data are available regarding a link between vascular changes and seizures (Nnode-Ekane et al., 2010). We found that the vasomotor phenomena of micro blood vessels correlate with interictal spike and wave discharges (Fig. 6d). Interictal spikes generated a strong cerebral metabolic change that induced cerebral vessel dilation and a focal increase in cerebral blood flow provided oxygenated hemoglobin to hypermetabolic neurons, with a corresponding increase in total hemoglobin (Ma et al., 2009). Vasomotion during seizure onset and spread was clearly caused by the oscillation in vessel diameter

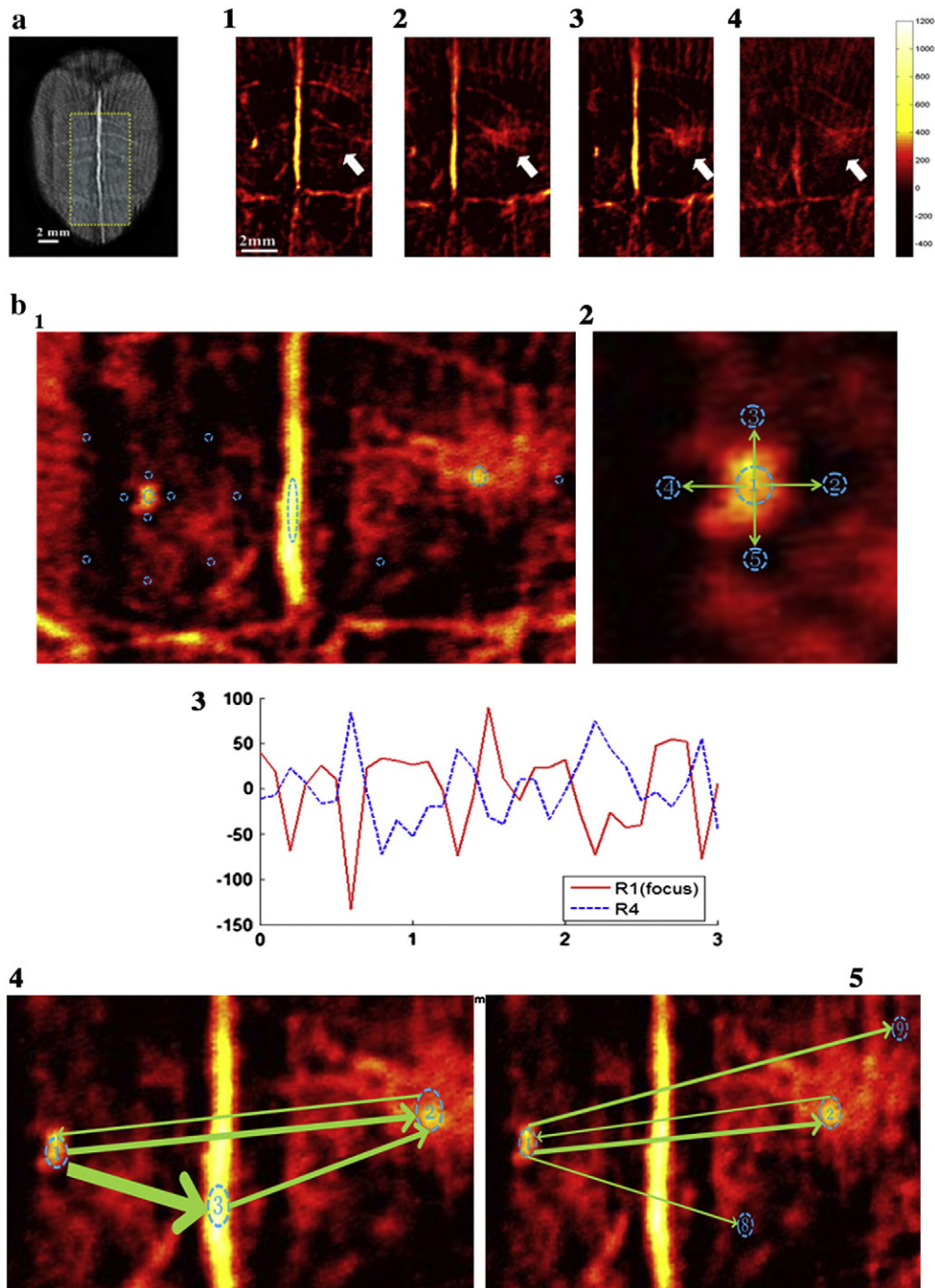


Fig. 5. *In vivo* maps of mirror foci propagation. (a.) Left, the PA image of the rat brain; the yellow dotted rectangular shows the ROI for analysis; Right, noninvasive imaging of the primary and mirror foci in bilateral homotopic cortex. a1–4 shows how mirror foci were generated and diminished. White arrow shows the location of mirror foci. The PA signal in the mirror foci was smaller in magnitude and delayed in time compared to the signal recorded from the primary foci. (b.) Granger analysis of seizure foci, mirror foci and middle cerebral artery; b1, a PAT image showing the nine selected ROIs; b2, Granger analysis of the image around the foci and its 'surround' area; b3, PA signal from the foci (red) and surround (blue) during an ictal event. The PA signal surrounding the foci (blue line) shows inverted signal compared to that from the seizure foci (red line) corresponding to neuronal inhibition. b4, connectivity relation between the primary and mirror focus; b5, connectivity relation between the primary focus, mirror focus and middle cerebral artery. The line width stands for the relative Granger causal influence strength. (For interpretation of the references to color in this figure legend, the reader is referred to the web of this article.)

and the expansion of the vessel cross section. We reasoned that the dilation resulted in an active cerebral microvasculature response to increased metabolic activity accompanying the seizure (Myers and Intaglietta, 1976). The combination of multi-scale imaging ability and endogenous hemoglobin contrast makes PAT a promising tool for imaging microvasculature during seizure onset. Future quantitative PAT studies will allow us to resolve many of the hemodynamic components, including changes in level of hemoglobin oxygenation (i.e., deoxy- and

oxy-hemoglobin), cerebral blood flow, and the rate of cerebral oxygen metabolism, for a detailed understanding of the neurovascular coupling phenomenon, both during and in between seizures (Yao et al., 2009; Yuan et al., 2007).

The present work represents a major technological and scientific improvement in epilepsy. Previous attempts to track from moment to moment populations of neurons participating in an epileptiform event had not been possible with any technique or tool because of

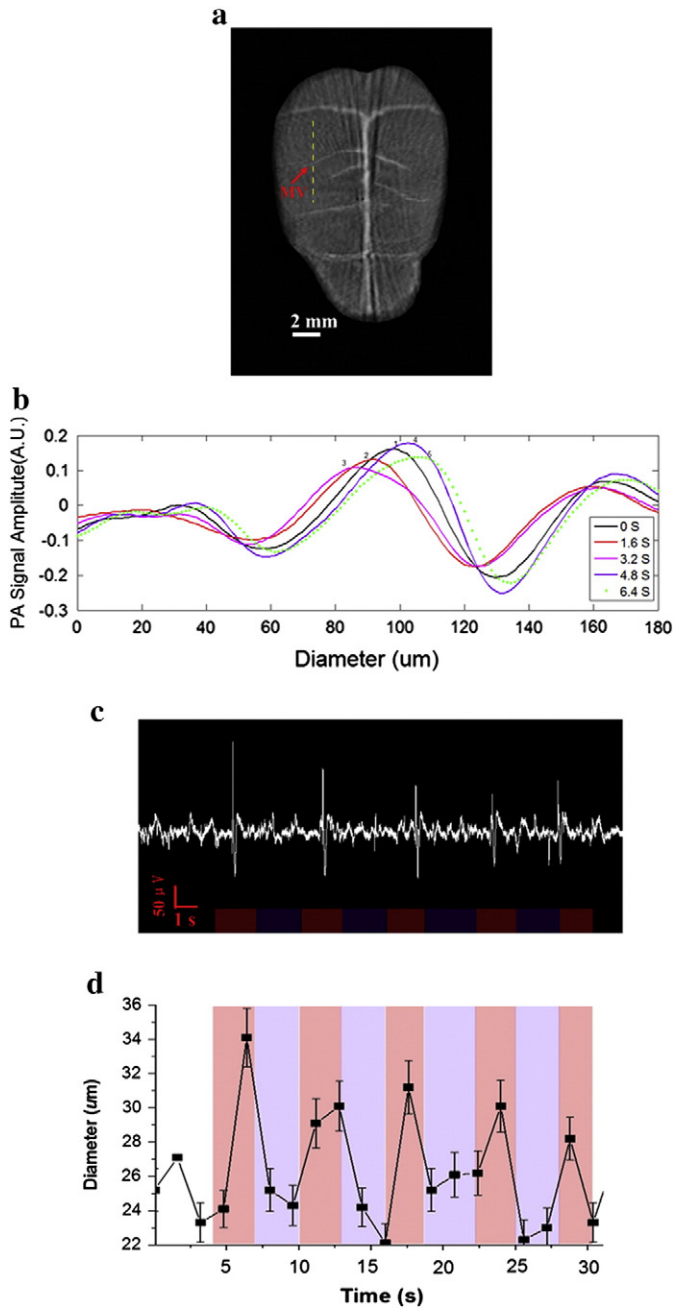


Fig. 6. Changes of blood vessel diameter during interictal onset. (a.) PA image of the rat cortex vasculature with the intact scalp and skull. The red arrow indicates the microvasculature (MV) along the yellow dashed line direction for a cross-sectional scanning using a 50 MHz ultrasound transducer. (b.) Typical photoacoustic signals from the targeted vessel at different times. (c.) EEG recordings show the interictal spikes and (d.) Change of the vessel size captured by PAT. Here was a clear correlation between the interictal spikes and the changes of the vessel size. Error bars (\pm s.d.) were calculated from 20 consecutive spikes. (For interpretation of the references to color in this figure legend, the reader is referred to the web of this article.)

spatial and/or temporal sampling limitations. The high spatial and temporal sampling of the novel PAT system allowed for the first time the complete mapping of an epileptiform event *in vivo*. Another major improvement is that this is the first report of mapping an epileptiform event at depths well below the cortex. In terms of impact, this is the first demonstration of emerging optical mapping tool in the surgical evaluation of focal cortical epilepsy, since accurate localization of the epileptic focus, propagation paths, and subcortical networks critically depends on the precise localization of epileptogenic neurons and networks. The use of our PAT system, experimental

paradigm, results, and analyses advances our understanding of epilepsy and seizure temporal spatial properties relative to previous attempts. The noninvasive yet whole surface and depth capabilities of the PAT system allowed for the first time to actually see what is happening during ictogenesis in terms of seizure onset and spread. The challenge of mapping focal epilepsy stems from the observation that the pathology associated with focal epilepsy is often distributed across a number of brain sites. Seizures in animal models and in people often have a multifocal or broadly synchronized onset. The implication of these observations is that each of the sites could act independently to initiate a seizure or, potentially, to drive another site into a seizure. The current study lends support to the theory that seizure onset and spread involves a rich interplay between multiple cortical and subcortical foci during the onset and spread of focal epilepsy. The findings are timely in the sense that the neuroscience community is questioning the long-held dogma that seizure onset involves some sort of single focus or epicenter in favor of the emerging thought that seizures instead involve multiple cortical and subcortical foci.

Acknowledgments

This research was supported in part by a grant from the US Department of Defense Congressionally Directed Medical Program, the B.J. and Eve Wilder endowment fund, and the Children's Miracle Network.

Appendix A. Supplementary data

Supplementary data to this article can be found online at <http://dx.doi.org/10.1016/j.neuroimage.2012.10.077>.

Reference

- Berg, A.T., Langfitt, J.T., Spencer, S.S., Vickrey, B.G., 2007. Stopping antiepileptic drugs after epilepsy surgery: a survey of U.S. epilepsy center neurologists. *Epilepsy Behav.* 10, 219–222.
- Bertram, E.H., 2009. Temporal lobe epilepsy: where do the seizures really begin? *Epilepsy Behav.* 14, 32–37.
- Bertram, E.H., Zhang, D.X., Mangan, P., Fountain, N., Rempe, D., 1998. Functional anatomy of limbic epilepsy: a proposal for central synchronization of a diffusely hyperexcitable network. *Epilepsy Res.* 32, 194–205.
- Birbeck, G.L., Hays, R.D., Cui, X., Vickrey, B.G., 2002. Seizure reduction and quality of life improvements in people with epilepsy. *Epilepsia* 43, 535–538.
- Bluestone, A.Y., Abdoulaev, G., Schmitz, C.H., Barbour, R.L., Hielscher, A.H., 2001. Three-dimensional optical tomography of hemodynamics in the human head. *Opt. Express* 9, 272–286.
- Boas, D.A., Gaudette, T., Strangman, G., Cheng, X., Marota, J.J., Mandeville, J.B., 2001. The accuracy of near infrared spectroscopy and imaging during focal changes in cerebral hemodynamics. *Neuroimage* 13, 76–90.
- Bressler, S.L., Tang, W., Sylvester, C.M., Shulman, G.L., Corbetta, M., 2008. Top-down control of human visual cortex by frontal and parietal cortex in anticipatory visual spatial attention. *J. Neurosci.* 28, 10056–10061.
- Brovelli, A., Ding, M., Ledberg, A., Chen, Y., Nakamura, R., Bressler, S.L., 2004. Beta oscillations in a large-scale sensorimotor cortical network: directional influences revealed by Granger causality. *Proc. Natl. Acad. Sci. U. S. A.* 101, 9849–9854.
- Cadotte, A.J., DeMarse, T.B., Mareci, T.H., Parekh, M.B., Talathi, S.S., Hwang, D.U., Ditto, W.L., Ding, M.Z., Carney, P.R., 2010. Granger causality relationships between local field potentials in an animal model of temporal lobe epilepsy. *J. Neurosci. Methods* 189, 121–129.
- Cendes, F., Cook, M.J., Watson, C., Andermann, F., Fish, D.R., Shorvon, S.D., Bergin, P., Free, S., Dubeau, F., Arnold, D.L., 1995. Frequency and characteristics of dual pathology in patients with lesional epilepsy. *Neurology* 45, 2058–2064.
- Denk, W., Strickler, J.H., Webb, W.W., 1990. Two-photon laser scanning fluorescence microscopy. *Science* 248, 73–76.
- Duncan, J.S., Sander, J.W., Sisodiya, S.M., Walker, M.C., 2006. Adult epilepsy. *Lancet* 367, 1087–1100.
- Engel, J., 2004. The goal of epilepsy therapy: no seizures, no side effects, as soon as possible. *CNS Spectr.* 9, 95–97.
- Folbergrová, J., Ingvar, M., Siesjö, B.K., 1981. Metabolic changes in cerebral cortex, hippocampus, and cerebellum during sustained bicuculline-induced seizures. *J. Neurochem.* 37, 1228–1238.
- Fountain, N.B., Bear, J., Bertram, E.H., Lothman, E.W., 1998. Responses of deep entorhinal cortex are epileptiform in an electrogenic rat model of chronic temporal lobe epilepsy. *J. Neurophysiol.* 80, 230–240.
- Granger, C.W.J., 1969. Investigating causal relations by econometric models and cross-spectral methods. *Econometrica* 37 (414–8).

- Greenfield, J., Geyer, J., Carney, P.R., 2011. Reading EEGs: a Practical Approach. Lippincott Wilkins Raven, Philadelphia.
- Grinvald, A., Frostig, R.D., Lieke, E., Hildesheim, R., 1988. Optical imaging of neuronal activity. *Physiol. Rev.* 68, 1285–1366.
- Haglund, M.M., Hochman, D.W., 2004. Optical imaging of epileptiform activity in human neocortex. *Epilepsia* 45, 43–47.
- Haglund, M.M., Ojemann, G.A., Hochman, D.W., 1992. Optical imaging of epileptiform and functional activity in human cerebral cortex. *Nature* 358, 668–671.
- Hauser, W.A., 1992. Seizure disorders: the changes with age. *Epilepsia* 33 (Suppl. 4), S6–14.
- Hauser, W.A., Annegers, J.F., Rocca, W.A., 1996. Descriptive epidemiology of epilepsy: contributions of population-based studies from Rochester, Minnesota. *Mayo Clin. Proc.* 71, 576–586.
- Hill, D.K., Keynes, R.D., 1949. Opacity changes in stimulated nerve. *J. Physiol. (Lond.)* 108, 278–281.
- Hu, S., Rao, B., Maslov, K., Wang, L.V., 2010. Label-free photoacoustic ophthalmic angiography. *Opt. Lett.* 35, 1–3.
- Huang, D., Swanson, E.A., Lin, C.P., Schuman, J.S., Stinson, W.G., Chang, W., Hee, M.R., Flotte, T., Gregory, K., Puliafito, C.A., Fujimoto, J.G., 1991. Optical coherence tomography. *Science* 254, 1178–1181.
- Institute, A.N.S., 2007. American national standard for the safe use of lasers. ANSI z136.1. Laser Institute of America, Orlando, Fla.
- Jeha, L.E., Najm, I., Bingaman, W., Dinner, D., Widdess-Walsh, P., Luders, H., 2007. Surgical outcome and prognostic factors of frontal lobe epilepsy surgery. *Brain* 130, 574–584.
- Jiang, H.B., Paulsen, K.D., Osterberg, U.L., Pogue, B.W., Patterson, M.S., 1996. Optical image reconstruction using frequency-domain data: simulations and experiments. *J. Opt. Soc. Am. A* 13, 253–266.
- Kaminski, M., Ding, M.Z., Truccolo, W.A., Bressler, S.L., 2001. Evaluating causal relations in neural systems: Granger causality, directed transfer function and statistical assessment of significance. *Biol. Cybern.* 85, 145–157.
- Khalilov, I., Holmes, G.L., Ben-Ari, Y., 2003. In vitro formation of a secondary epileptogenic mirror focus by interhippocampal propagation of seizures. *Nat. Neurosci.* 6, 1079–1085.
- Kruger, R.A., Liu, P.Y., 1994. Photoacoustic ultrasound – pulse production and detection in 0.5-percent liposyn. *Med. Phys.* 21, 1179–1184.
- Laufer, J., Delpy, D., Elwell, C., Beard, P., 2007. Quantitative spatially resolved measurement of tissue chromophore concentrations using photoacoustic spectroscopy: application to the measurement of blood oxygenation and haemoglobin concentration. *Phys. Med. Biol.* 52, 141–168.
- Ma, H., Zhao, M., Suh, M., Schwartz, T.H., 2009. Hemodynamic surrogates for excitatory membrane potential change during interictal epileptiform events in rat neocortex. *J. Neurophysiol.* 101, 2550–2562.
- Mace, E., Montaldo, G., Cohen, I., Baulac, M., Fink, M., Tanter, M., 2011. Functional ultrasound imaging of the brain. *Nat. Methods* 8, 662–U685.
- Mangan, P.S., Scott, C.A., Williamson, J.M., Bertram, E.H., 2000. Aberrant neuronal physiology in the basal nucleus of the amygdala in a model of chronic limbic epilepsy. *Neuroscience* 101, 377–391.
- Myers, R.R., Intaglietta, M., 1976. Brain microvascular hemodynamic responses to induced seizures. *Stroke* 7, 83–88.
- Ndode-Ekane, X.E., Hayward, N., Grohn, O., Pitkanen, A., 2010. Vascular changes in epilepsy: functional consequences and association with network plasticity in pilocarpine-induced experimental epilepsy. *Neuroscience* 166, 312–332.
- Ogawa, S., Lee, T.M., Nayak, A.S., Glynn, P., 1990. Oxygenation-sensitive contrast in magnetic-resonance image of rodent brain at high magnetic-fields. *Magn. Reson. Med.* 14, 68–78.
- Oleary, M.A., Boas, D.A., Chance, B., Yodh, A.G., 1995. Experimental images of heterogeneous turbid media by frequency-domain diffusing-photon tomography. *Opt. Lett.* 20, 426–428.
- Paxinos, G.W.C., 1998. *The Rat Brain*. Academic Press.
- Schwartz, T.H., Bonhoeffer, T., 2001. *In vivo* optical mapping of epileptic foci and surround inhibition in ferret cerebral cortex. *Nat. Med.* 7, 1063–1067.
- Shelton, R.L., Applegate, B.E., 2010. Ultrahigh resolution photoacoustic microscopy via transient absorption. *Biomed. Opt. Express* 1, 676–686.
- Sipkins, D.A., Wei, X.B., Wu, J.W., Runnels, J.M., Cote, D., Means, T.K., Luster, A.D., Scadden, D.T., Lin, C.P., 2005. In vivo imaging of specialized bone marrow endothelial microdomains for tumour engraftment. *Nature* 435, 969–973.
- Sokol, D.K., Markand, O.N., Daly, E.C., Luerssen, T.G., Malkoff, M.D., 2000. Near infrared spectroscopy (NIRS) distinguishes seizure types. *Seizure* 9, 323–327.
- Steinhoff, B.J., Herrendorf, G., Kurth, C., 1996. Ictal near infrared spectroscopy in temporal lobe epilepsy: a pilot study. *Seizure* 5, 97–101.
- Thom, M., Mathem, G.W., Cross, J.H., Bertram, E.H., 2010a. Mesial temporal lobe epilepsy: how do we improve surgical outcome? *Ann. Neurol.* 68, 424–434.
- Thom, M., Mathern, G.W., Cross, J.H., Bertram, E.H., 2010b. Mesial temporal lobe epilepsy: how do we improve surgical outcome? *Ann. Neurol.* 68, 424–434.
- Wang, X., Chen, Y.H., Bressler, S.L., Ding, M.Z., 2007. Granger causality between multiple interdependent neurobiological time series: blockwise versus pairwise methods. *Int. J. Neural Syst.* 17, 71–78.
- Watanabe, E., Maki, A., Kawaguchi, F., Yamashita, Y., Koizumi, H., Mayanagi, Y., 2000. Noninvasive cerebral blood volume measurement during seizures using multichannel near infrared spectroscopic topography. *J. Biomed. Opt.* 5, 287–290.
- Xiang, L.Z., Xing, D., Gu, H.M., Yang, D.W., Yang, S.H., Zeng, L.M., Chen, W.R., 2007. Real-time optoacoustic monitoring of vascular damage during photodynamic therapy treatment of tumor. *J. Biomed. Opt.* 12.
- Yang, S.H., Xing, D., Lao, Y.Q., Yang, D.W., Zeng, L.M., Xiang, L.Z., Chen, W.R., 2007. Non-invasive monitoring of traumatic brain injury and post-traumatic rehabilitation with laser-induced photoacoustic imaging. *Appl. Phys. Lett.* 90.
- Yao, L., Sun, Y., Jiang, H.B., 2009. Quantitative photoacoustic tomography based on the radiative transfer equation. *Opt. Lett.* 34, 1765–1767.
- Yuan, Z., Wang, Q., Jiang, H.B., 2007. Reconstruction of optical absorption coefficient maps of heterogeneous media by photoacoustic tomography coupled with diffusion equation based regularized Newton method. *Opt. Express* 15, 18076–18081.
- Zhang, Q.Z., Liu, Z., Carney, P.R., Yuan, Z., Chen, H.X., Roper, S.N., Jiang, H.B., 2008. Non-invasive imaging of epileptic seizures in vivo using photoacoustic tomography. *Phys. Med. Biol.* 53, 1921–1931.